

JAMES Journal of Advances in Modeling Earth Systems



RESEARCH ARTICLE

10.1029/2019MS001904

Key Points:

- Anisotropic eddy diffusivity is diagnosed with a multiple tracers inversion technique
- An eigendecomposition of the horizontal diffusion tensor determines the 3-D parameterized transport
- This diagnosis informs an anisotropic extension to the GM-Redi parameterization

Correspondence to:

S. D. Bachman, bachman@ucar.edu

Citation:

Bachman, S. D., Fox-Kemper, B., & Bryan, F. O. (2020). A diagnosis of anisotropic eddy diffusion from a high-resolution global ocean model. *Journal of Advances in Modeling Earth Systems*, *12*, e2019MS001904. https://doi.org/10.1029/2019MS001904

Received 20 SEP 2019 Accepted 12 JAN 2020 Accepted article online 14 JAN 2020

©2020. The Authors. This is an open access article under the terms of the Creative Commons Attribution-NonCommercial-NoDerivs License, which permits use and distribution in any medium, provided the original work is properly cited, the use is non-commercial and no

modifications or adaptations are made.

A Diagnosis of Anisotropic Eddy Diffusion From a High-Resolution Global Ocean Model

Scott D. Bachman¹, Baylor Fox-Kemper², and Frank O. Bryan¹

¹National Center for Atmospheric Research, Boulder, CO, USA, ²Department of Earth, Environmental, and Planetary Sciences, Brown University, Providence, RI, USA

Abstract Oceanic mesoscale eddies are known to diffuse and stir tracers, and the development of skillful eddy closures is aided considerably by the accurate diagnosis of these processes from eddy-resolving model statistics. In this work a multiple-tracers inversion method is applied to a global mesoscale eddy-resolving simulation, with the intent to solve for the eddy transport tensor that describes the eddy diffusion (symmetric part) and stirring (antisymmetric part). Special emphasis is placed on diagnosing the anisotropy of the horizontal transport, which is described by the eigenvalues and eigenvectors of the 2×2 horizontal symmetric subtensor. Global diagnoses of these quantities, along with an examination of their vertical structures, are used to recommend an algorithm for extending the Gent and McWilliams and Redi parameterizations to include anisotropic effects.

Plain Language Summary Tracer transport by ocean mesoscale eddies is usually parameterized using a flux-gradient relationship with a scalar transport coefficient for the horizontal fluxes. Using a scalar coefficient implies that the transport is horizontally isotropic. There exist many mechanisms that may lead to anisotropic transport, however, and parameterizing this anisotropy requires a (symmetric) tensor coefficient. We diagnose this tensor coefficient using a high-resolution global ocean model with an inversion method that uses multiple passive tracers. The statistics from the diagnosis allow us to explore the properties of the flow that govern the anisotropy, and to recommend an anisotropic extension of extant tracer parameterization schemes.

1. Introduction

Mesoscale eddies play a dominant role in the transport of heat, salt, and tracers in the world ocean (Bryden & Brady, 1989; Chelton et al., 2011; McGillicuddy et al., 2007) and occupy a range of scales from 10 to 500 km depending on latitude, bathymetry, atmospheric state, and stratification (Chelton et al., 2007). The properties of tracer transport by these eddies have been of longstanding interest to the oceanographic community, where the transport is generally conceived as a combination of irreversible mixing, or diffusion, and reversible stirring, or advection. Mesoscale eddies themselves do not mix tracers (Bryan & Bachman, 2015); rather, stirring occurs as the eddies strain and fold the tracer isolines, and only after analyzing the bulk characteristics of the Lagrangian decorrelation of the tracer is the transport usefully approximated as eddy "diffusion." The conception of eddy transport as a diffusive process has been used to describe the broad behavior of eddies over a wide variety of flow regimes (Kraichnan, 1987) and has spurred the development of techniques and observational tools to quantify the efficiency of the eddy transport (i.e., the "eddy diffusivity"; Abernathey et al., 2013; Davis, 1987; Mak et al., 2016; Nakamura, 2001; Wolfram et al., 2015).

In reality, the diffusive model hides a variety of mechanisms that can strain or stir water parcels in different ways, such as shear disperson (Okubo, 1967; Smith, 2005; Taylor, 1953, 1954; Young et al., 1982), transport across jets (Ferrari & Nikurashin, 2010; Rogerson et al., 1999), or topographic influences (LaCasce & Speer, 1999). Simply using a scalar "eddy diffusivity" avoids these details and implicitly assumes that the above mechanisms are either infrequent or unimportant enough to not warrant concern.

The standard practice in ocean modeling is to parameterize mesoscale eddy fluxes as a linear combination of the local directional derivatives of the tracer (e.g., employ a flux-gradient relationship; Vallis, 2017). In multiple dimensions the magnitude of the fluxes is governed by an eddy transport tensor, **K**, where the word "transport" is used in lieu of "diffusion" to acknowledge that the transport is both advective (antisymmetric part) and diffusive (symmetric part) in nature (e.g., Griffies, 1998). Transport in the oceanic interior occurs

BACHMAN ET AL. 1 of 24



primarily along neutral buoyancy surfaces (McDougall, 1987) that are tilted with respect to the horizontal, and this tilting must be accounted for in a non-isopyncal model. The weights on each directional derivative in the flux-gradient relationship are therefore functions of the angle between the isoneutral slope and the local coordinate surface, and the transport is anisotropic in that it distinguishes transport across neutral planes as being much weaker than along them.

Typical implementations of the flux-gradient approach use a combination of the Gent and McWilliams (1990, hereafter GM) and Redi (1982) schemes for neutral advection and diffusion, respectively, where the magnitude is set by a transversely isotropic transport coefficient (i.e., isotropic within the neutral plane). A significant body of literature exists, which establishes theory and diagnostic techniques for specifying the transport coefficient (e.g., Cessi, 2008; Eden & Greatbatch, 2008; Killworth, 1997; Marshall et al., 2012; Visbeck et al., 1997). However, many of these approaches are only formally applicable when applied along one dimension or when the eddy transport is nearly isotropic, thereby reducing the effective dimension of the transport.

An extension of the tensor-based, tracer flux-gradient parameterization approach that introduces horizontal anisotropy was formulated by Smith and Gent (2004). The essence of this "anisotropic GM" parameterization is it allows the subgrid-scale physics to have a preferred direction that may not be aligned with the model grid, and along which the transport may be enhanced. Diagnosing a single, scalar transport coefficient is thus no longer sufficient to inform the eddy transport operator in this approach; rather, *each element* of **K** must be diagnosed and further tensor algebra must be used to untangle the directionality and magnitude of the transport—in the horizontal as well as the vertical. Both Eulerian (e.g., Bachman & Fox-Kemper, 2013; Bachman et al., 2015) and Lagrangian (e.g., Wolfram et al., 2015) diagnostic techniques have been developed that are well suited to this task. A key advantage of this extension to anisotropy is that eddy fluxes need not be aligned with the tracer gradients—indeed that is the exception, even though the diffusive and advective character of the eddy transport is preserved.

This paper will focus on the Eulerian diagnosis of the eddy transport tensor through analysis of the transport of multiple tracers, with a particular emphasis on the horizontal anisotropy of eddy diffusion. Mathematically this implies an analysis of only the symmetric part of \mathbf{K} , and a focus on its 2×2 horizontal subtensor. We note that this transport is not strictly horizontal and it would be more accurate to call it epineutral, but in practice, this distinction is small (unlike the dianeutral transport, which must be carefully diagnosed in only that direction). Fox-Kemper et al. (2013) discussed many implications of anisotropic eddy transport and presented an earlier version of this diagnosis in comparison to a similar analysis using surface drifters but without the present focus on the horizontal symmetric tensor. This work aims to present an updated version of their analysis, except with a proper tensor decomposition and using improved diagnostic techniques that better account for the consequences of dissipation of tracer anomalies in the analysis (Bachman et al., 2015). Though the horizontal symmetric tensor is explicitly *not* part of the GM transport, the GM transport is mathematically related (Smith & Gent, 2004). This relationship will be exploited so that, via emphasis on only the horizontal symmetric tensor, a roadmap is created by which an anisotropic GM-Redi parameterization can be realized.

This paper is organized as follows. Section 2 introduces the theory of the flux-gradient parameterization in tensor form and its anisotropic extension. Section 3 discusses the high-resolution global model used for the tensor diagnosis and the techniques that will be used. Section 4 presents the results of the diagnosis and implications for building the anisotropic GM-Redi parameterization. Concluding remarks appear in section 5.

2. The Anisotropic Eddy Transport Tensor

Passive tracers are useful for understanding eddy transport because their distribution has no impact on the evolution of the flow in which they reside, so many can be used simultaneously to extract information about the transport without affecting it. That is, in an unforced eddying regime variations in the tracer concentration can be assumed to be the result of turbulent processes and not due to feedbacks from the tracer onto the flow itself. For example, consider the conservation equation for a passive tracer τ :

$$\frac{\partial \tau}{\partial t} + \mathbf{u} \cdot \nabla \tau = \mathcal{F},\tag{1}$$

BACHMAN ET AL. 2 of 24

where $\mathbf{u} = (u, v, w)$ is the three-dimensional velocity vector and any nonconservative sources and sinks of tracer concentration are wrapped into the variable \mathcal{F} . The chaotic nature of turbulence makes predicting the evolution of τ a nearly impossible task except in the most idealized flow geometries. Rather, a standard approach is to assume there exists some spatiotemporal scale at which eddies collectively exhibit some kind of systematic behavior (permitting a Reynolds averaging in time or filtering in space), meaning that one is no longer examining individual eddy fluxes but rather their ensemble (mean) statistics. For simplicity we make the assumption that the mean and eddy scales are sufficiently distinct to warrant a Reynolds averaging, while cautioning that this assumption of scale separation is invalid for nearly all modern ocean models (such models are properly considered as large-eddy simulations [e.g., Fox-Kemper & Menemenlis, 2008], but doing so complicates the averaging procedure, introduces cross-scale correlation terms into (2), and unnecessarily distracts from the discussion here). After averaging (1) becomes

$$\frac{\partial \bar{\tau}}{\partial t} + \mathbf{u} \cdot \nabla \bar{\tau} = \bar{F} - \nabla \cdot \overline{\mathbf{u}' \tau'}.$$
 (2)

The variables with the overbar refer to the mean fields (which are normally related to the resolved fields in a coarse resolution model without eddies), and the eddy components are denoted by a prime. By definition, the eddy components do not have a mean, but their covariances with tracers do not vanish upon averaging and can affect the mean tracer concentrations through these transports, which are thus related to the eddy transports that are missing in coarse resolution models. For the special case when $\mathcal{F}=0$ the lack of material conservation of the mean tracer budget following the mean flow is then entirely due to eddy effects, which are captured in the eddy flux divergence term on the right side of (2).

Another advantage of assuming scale separation is that it allows eddy perturbations to be expressed using Taylor expansions, that is, using mixing length theory (e.g., Taylor, 1922; Vallis, 2017) to write

$$\tau' = -l_x' \partial_x \bar{\tau} - l_y' \partial_y \bar{\tau} - l_z' \partial_z \bar{\tau} - \frac{1}{2} l_x'^2 \partial_{xx} \bar{\tau} - \frac{1}{2} l_x' l_y' \partial_{xy} \bar{\tau} - \frac{1}{2} l_x' l_z' \partial_{xz} \bar{\tau} \dots$$
 (3)

for directional parcel excursions l'_x , l'_y , and l'_z . Because the perturbation scale is small compared to the scale over which $\bar{\tau}$ varies, to leading order the averaged eddy tracer fluxes can be expressed as

$$\overline{\mathbf{u}'\tau'} = -\mathbf{K}\cdot\nabla\bar{\tau},\tag{4}$$

where the second-order tensor K consists of the covariances between the eddy velocities and displacements,

$$K_{ij} \approx \overline{u'_i l'_j},$$
 $(i, j) = \{1, 2, 3\}.$ (5)

and the indices i and j denote the three spatial dimensions.

A key point in (4) is that the elements of **K** are seen to be independent of the tracer concentration; that is, they are composed of correlations between eddy velocity and length scales but are not functions of the tracer itself. For this reason the same **K** can be assumed to apply to all passive tracers in parameterizations, and any tracer dependence in (4) is captured in the tracer gradient. Note, however, that the Eulerian transport model in (5) does not imply that **K** is symmetric (i.e., $K_{ij} \neq K_{ji}$), as is suggested by the Lagrangian diffusion model of Taylor (1922) and Batchelor (1949). It is the difference between the Lagrangian and Eulerian frameworks that accounts for the discrepancy, that is, the advective "quasi-Stokes" component of the transport that results from thickness-velocity correlations and that cannot be represented diffusively (Dukowicz & Smith, 1997; Griffies, 1998; Plumb & Ferrari, 2005).

Writing the elements of **K** in the form (5) makes it apparent that anisotropic transport arises through directional differences in the eddy velocity, the eddy length scale, or their correlation (e.g., if $u_1' >> u_2'$, or similarly for the parcel excursions **l'**). Effects that directionally suppress eddy perturbations, such as the presence of a strong potential vorticity (PV) gradient due to a jet (Ferrari & Nikurashin, 2010) or steep bathymetry (Isachsen, 2011; Mechoso, 1980), reduce the magnitude of the K_{ij} eigenvector associated with that direction. The steering of the eddy fluxes is thus manifested in the structure of **K**, its eigenvalues, and eigenvectors.

The full transport tensor \mathbf{K} is a composition of both advective and diffusive transports, each of which has distinct mathematical properties. Therefore, a proper analysis must consider each of these transports in isolation. As a square matrix, \mathbf{K} can be decomposed into the sum of a symmetric tensor, \mathbf{S} , and an antisymmetric tensor, \mathbf{A} , so (4) can also be written

BACHMAN ET AL. 3 of 24

$$\overline{\mathbf{u}'\tau'} = -(\mathbf{A} + \mathbf{S}) \cdot \nabla \bar{\tau} \tag{6}$$

$$\mathbf{A} \equiv \frac{1}{2} \left(\mathbf{K} - \mathbf{K}^T \right) \tag{7}$$

$$\mathbf{S} \equiv \frac{1}{2} \left(\mathbf{K} + \mathbf{K}^T \right), \tag{8}$$

where T represents the transpose of the matrix. The physics of the full transport tensor **K** can be understood by examining its symmetric and antisymmetric parts separately.

Here we will focus special attention on the symmetric tensor, S, which retains its symmetry under any coordinate transformation. A physically based, general approach would be to describe S by its eigenvalues and eigenvectors, which satisfy the relation

$$\mathbf{S} \cdot \mathbf{v}_i = \kappa_i \mathbf{v}_i, \qquad i = \{1, 2, 3\}. \tag{9}$$

The eigenvalues of a symmetric, real tensor are always real. If the eigenvalues of a symmetric tensor are all nonnegative, then they are all nonnegative under any continuous coordinate transformation, including stretching, rotating, and partially aligning the basis vectors. Furthermore, if the eigenvalues are all nonnegative, then the tensor acts on the tracer gradient to reduce the total tracer variance, and thus, the transport is diffusive in nature (Griffies et al., 1998). Each eigenvalue comes with an eigenvector, whose direction denotes where the full matrix operator behaves like a scalar diffusivity. For symmetric tensors, these eigenvectors are orthogonal even if the coordinate basis is not. For oceanic flow the eigenvectors associated with the dominant eigenvalues tend to be oriented in and span the epineutral plane, so that the eigenvector associated with the smallest (or zero) eigenvalue is typically dianeutral.

Diffusion occurs in the direction of each of the eigenvectors, \mathbf{v}_i , which jointly form an orthonormal basis called the principal axes of \mathbf{S} , and the diffusivity along each axis is given by the corresponding eigenvalue κ_i . The eigenvalues do not necessarily have to be positive (i.e., diffusive down gradients oriented along the corresponding eigenvector); indeed, well-known examples exist in geophysical fluids where transport can be upgradient (e.g., Starr, 1966; Wilson & Williams, 2006), though from the perspective of parameterization development the numerical stability of upgradient closures is doubtful. For 2×2 tensors we will define the major axis to be that which corresponds to the larger eigenvalue by absolute value and the minor axis to be associated with the smaller eigenvalue. For the full 3×3 tensor, these will be the largest and middle eigenvalue, respectively.

It is important to note that in general a symmetric tensor diffusivity is not perfectly downgradient. In fact, perfectly downgradient diffusion can only occur in two cases. The first case occurs if $\bf S$ has only one nonzero eigenvalue whose eigenvector direction is aligned with the gradient of the tracer being diffused. If the gradient is oriented in another direction and has a nonzero projection onto more than one of the eigenvector directions with unequal eigenvalues, then the components of the gradient along each of the principal axes of diffusion will be diffused at different rates and the net transport will not align with the tracer gradient. The second case is that of isotropic diffusion where some of the eigenvalues are equal, and then the effect of the symmetric tensor on any tracer gradient within the plane or volume span of the eigenvectors with equal eigenvalues is the same as multiplication by a scalar diffusivity (equal to the shared eigenvalue). In general, tracers are likely to be diffused anisotropically by large-scale oceanic motions, where a variety of effects—such as gravity, topography, mean flows, and zonal versus meridional distinctions—break the symmetries of mixing irrespective of any other kinematic effects that may render each κ unequal (Fox-Kemper et al., 2013).

2.1. The "Ordinary" Anisotropy of Dianeutral Versus Epineutral Diffusivity

The construction of the GM-Redi theory distinguishes the directions where fluxes will occur along and across neutral density surfaces (or more sophisticated thermodynamic quantities if one prefers). This means that the Redi tensor is already anisotropic, with two large eigenvalues in the epineutral plane and one small, or zero, eigenvalue in the dianeutral direction. This idea extends back to Welander (1971) and Veronis (1975), and it results physically from the relatively low energy density of the mesoscale versus the high potential energy required to overturn stable stratification (i.e., the very large Richardson number of mesoscale flows). It is an important anisotropy to preserve in order to avoid spurious mixing of water masses.

BACHMAN ET AL. 4 of 24



2.2. Anisotropy Within the Epineutral Plane

Motion in the ocean interior occurs primarily along neutral buoyancy surfaces, which are generally tilted with respect to surfaces of constant depth. Redi (1982) used a series of tensor transformations to rotate an isotropic diffusion tensor from density coordinates to z coordinates, in which the isoneutral slopes $\mathbf{L} = -\nabla_h \bar{b}/\partial_z \bar{b}$ are introduced as part of the coordinate transformation. A generalized version of this transformation was derived by R. D. Smith (1999, Appendix B); assuming no dianeutral diffusion, this epineutral diffusion tensor is

$$\mathbf{S} = \begin{bmatrix} \mathbf{S}_{H} & \mathbf{S}_{H} \cdot \mathbf{L} \\ (\mathbf{S}_{H} \cdot \mathbf{L})' & \mathbf{L} \cdot \mathbf{S}_{H} \cdot \mathbf{L} \end{bmatrix} \qquad \mathbf{S}_{H} = \begin{bmatrix} S_{xx} & S_{xy} \\ S_{xy} & S_{yy} \end{bmatrix}. \tag{10}$$

The horizontal 2×2 diffusion tensor \mathbf{S}_H is symmetric and determines the structure of the full 3-D tensor \mathbf{S} , since the terms in the third row and columns are simply the product of \mathbf{S}_H with the isoneutral slope vector. Likewise, Smith and Gent (2004) derived a form for a generalized, anisotropic antisymmetric tensor

$$\mathbf{A} = \begin{bmatrix} \mathbf{0}_{2\times2} & -\mathbf{S}_{H}^{*} \cdot \mathbf{L} \\ (\mathbf{S}_{H}^{*} \cdot \mathbf{L})' & 0 \end{bmatrix}, \tag{11}$$

where $\mathbf{0}_{2\times 2}$ is the 2×2 zero matrix and \mathbf{S}_H^* is a 2×2 symmetric tensor that is not necessarily equal to \mathbf{S}_H . For now the discussion will focus on the symmetric tensor (10) and will return to the relationship between \mathbf{S}_H and \mathbf{S}_H^* in section 4.

The advantage of expressing the diffusion tensors as in (10) is that it greatly simplifies the problem of diagnosing the eigenvalues and eigenvectors of S. To see this, consider the anisotropic diffusion tensor written in the isoneutral coordinate system:

$$\mathbf{S}_{I} = \begin{bmatrix} \mathbf{S}_{H} & \mathbf{0}_{2\times 1} \\ \mathbf{0}'_{2\times 1} & \epsilon \end{bmatrix}, \tag{12}$$

where now a dianeutral diffusivity ϵ has been included (upon coordinate rotation \mathbf{S}_I is equivalent to (10) in the limit $\epsilon=0$). It is simple to show using the method of expansion by minors that the eigenvalues of \mathbf{S}_I are the two eigenvalues of \mathbf{S}_H along with ϵ . To obtain the z coordinate tensor, \mathbf{S} , one must rotate \mathbf{S}_I using the tensor multiplication:

$$\mathbf{S} = \mathbf{R} \cdot \mathbf{S}_I \cdot \mathbf{R}^{-1},\tag{13}$$

where \mathbf{R} is a double rotation matrix with determinant one (Redi, 1982). Since the determinant of a product of matrices is the product of their determinants, this implies that the characteristic polynomials for \mathbf{S} and \mathbf{S}_I satisfy the relation:

$$\det \left[\mathbf{S} - \kappa \mathbf{I} \right] = \det \left[\mathbf{R} \cdot \left(\mathbf{S}_{I} - \kappa \mathbf{I} \right) \cdot \mathbf{R}^{-1} \right]$$
(14)

$$= \det \left[\mathbf{S}_I - \kappa \mathbf{I} \right]. \tag{15}$$

The equivalence of these polynomials means that the eigenvalues of S are the same as those for S_I . This implies that the epineutral anisotropy of S is entirely described by an eigendecomposition of S_H , and diagnosing the anisotropy reduces to solving a simple 2-D eigenvalue problem. We will henceforth use the term "horizontal" in place of "epineutral," as the former is more intuitive for the z coordinate models in which this analysis applies. We note that there is a small-slope approximation implicit in treating epineutral and horizontal as interchangeable (i.e., the cosine of the isopycnal tilt is approximately 1), but direct agreement of the eigenvalues and eigenvector orientations of the middle and largest eigenvalues of the 3×3 tensor and the large and small eigenvalues and eigenvectors of the 2×2 justifies this imprecise terminology.

It is clear that techniques traditionally used to diagnose a scalar κ are insufficient to diagnose the four elements of \mathbf{S}_H . However, recent work by Bachman et al. (2015) has led to a set of diagnostic techniques well suited for the determination of multiple tensor elements, which has thus far been successfully applied to determine two-dimensional diffusion and overturning in idealized channel flows (Abernathey et al.,

BACHMAN ET AL. 5 of 24



2013; Bachman & Fox-Kemper, 2013) in the plane perpendicular to the along-channel axis and are superior to the three-dimensional analysis techniques used in Fox-Kemper et al. (2013). The focus here is on a three-dimensional diagnostic inversion—diagnosing \mathbf{S}_H , the orientation of its principal axes, and magnitude of the associated eigenvalues—in a global eddy-resolving model, emphasizing the heterogeneity and anisotropy of horizontal diffusion. In the forthcoming sections the new inversion techniques will be reapplied to the same model as was used in Fox-Kemper et al. (2013), and the results will be leveraged to propose an anisotropic extension to the GM-Redi scheme.

3. The Global Diagnosis of S_H

3.1. Model Description and Experimental Design

The high-resolution global simulation used in this analysis was performed with the Parallel Ocean Program Version 2 (POP2) (Smith et al., 2010). This is a free surface hydrostatic primitive equation model discretized using a general orthogonal horizontal grid and level coordinates in the vertical. The horizontal dipole-type grid (Smith et al., 1995) has the northern grid pole displaced into North America with a zonal resolution of 0.1° and nominal meridional resolution of 0.1° cos(latitude). The configuration for this experiment is similar in most respects to that of Maltrud & McClean (2005, hereafter MM05) but departs from the MM05 configuration in the use of partial bottom cells (Adcroft et al., 1997) to provide a more accurate representation of topography. Two additional abyssal levels have been added as well, so that in total there are 42 levels in the vertical with 10-m resolution at the surface, stretching to 250 m in the abyss with a maximum depth of 6,000 m. A biharmonic subgrid-scale closure is used in the horizontal with the hyperdiffusivity and hyperviscosity scaled with the cube of the local grid length and equatorial (maximum) values of -9×10^9 m²/s and -2.7×10^{10} m⁴/s, respectively. The K-profile parameterization (Large et al., 1994) is used to represent surface boundary layer and interior diapycnal mixing. The background vertical diffusivity and viscosity increase from 0.1×10^{-4} m²/s in the upper ocean to 1.0×10^{-4} m²/s in the abyss.

Because the focus of the experiments is on isolating the transport properties of transient motions associated with mesoscale, we filter the surface forcing to retain only a mean annual cycle. The same input data sets as described in Maltrud and McClean (2005) were used after forming climatological monthly means. The surface wind stress was first computed off-line from the original daily varying winds and stability dependent drag coefficients. Note that the surface current was not used in the stress calculation. Surface heat and freshwater fluxes were computed from a combination of National Centers for Environmental Prediction/National Center for Atmospheric Research reanalysis estimates of the surface meteorological state and remote sensing products for downward radiation and precipitation fluxes. Surface temperature and salinity were strongly restored (timescale of 5 days) to their climatological monthly mean in regions with observed sea ice, and salinity was weakly restored at the surface elsewhere.

The integration was initialized at rest with potential temperature and salinity interpolated to the model grid from the World Ocean Atlas climatology (Antonov & Levitus, 2006; Locarnini et al., 2013). After 13 years of spin-up using the forcing described above, a suite of passive tracers was introduced for use in the transport tensor inversion. Three sets of three tracers were initialized with the following distributions:

$$\tau_1 = \tau_4 = \tau_7 = \frac{\phi}{90} \tag{16}$$

$$\tau_2 = \tau_5 = \tau_8 = \sin\frac{\pi\rho}{180} \tag{17}$$

$$\tau_3 = \tau_6 = \tau_9 = \frac{z_{max} - 2z}{z_{max}},\tag{18}$$

where ρ and ϕ are the longitude and latitude in degrees, respectively, z is depth, and $z_{max} = 6,000$ m. The concentration of each tracer thus varies over the range [-1,1]. During integration tracer sets $\{1,2,3\}$ and $\{4,5,6\}$ are damped back toward their initial conditions on timescales of 180 and 360 days, respectively, while tracer set $\{7,8,9\}$ is undamped. The model was integrated forward with these passive tracers for 10 years.

BACHMAN ET AL. 6 of 24



Several solutions for the passive tracer concentrations, velocities, state variables, and fluxes were saved by time averaging over years 16 to 23 of the simulation. Spatial averaging was also performed over an integer number of grid cells of the original 0.1° grid in the horizontal dimensions only. The solutions shown in this work use an average over 20 × 20 fine grid cells, yielding a coarsened grid with nominal resolution of 2°. This resolution is significantly coarser than the first baroclinic deformation radius at all latitudes except immediately at the equator (Hallberg, 2013), which makes the mean and eddy scales sufficiently separated to justify the flux-gradient approach (4). The averaging operation is mass conserving; that is, the mass within each coarsened grid cell is the same as the sum of the masses of each cell that contributed to the average. The averaging thus conserves the globally integrated tracer concentration as well. The coarsened mean fluxes and tracer gradients are constructed using the direct analogues of the fine-grid advection operators with the appropriately coarsened grid metric factors. Hereafter, quantities with an overbar will indicate the combination of this space and time averaging, and primes the deviation from this average.

3.2. Diagnosis Techniques

The diagnosis of ${\bf K}$ using the flux-gradient relationship (4) is problematic because it is an underdetermined system under only one tracer. That is, for a given tracer τ , the three elements of $\overline{{\bf u}'\tau'}$ and $\nabla\bar{\tau}$ do not provide enough constraints to uniquely solve for all nine elements of ${\bf K}$. The situation is further complicated by extra degrees of freedom hidden within the Reynolds-averaging operator that mask spatiotemporal variability in the eddy correlations. Therefore, to obtain an accurate solution for each member of ${\bf K}$ requires sampling a minimum of three tracers that are assumed to have the same ${\bf K}$ (yielding 3×3 matrices for both the fluxes and gradients) over a sufficient number of eddy realizations to smooth out this variability. The key principle behind this multiple-tracers inversion method is that it is unlikely that the averaging operator is coarse enough in space and time to achieve the required smoothness using only three tracers; rather, one can obtain the sufficient number of eddy realizations by employing extra tracers and (pseudo)inverting the resulting tracer gradient matrix. The goal of the pseudoinversion (denoted by a † superscript) is an accurate estimate of the eddy transport tensor, which in its simplest form (Bachman & Fox-Kemper, 2013) is calculated as

$$K_{ij} = -\overline{u_i'\tau_{\beta}'} \left[\bar{\tau}_{\beta,j}\right]^{\dagger}. \tag{19}$$

In this expression Einstein notation is employed, where i and j are used to index the three spatial dimensions and β is used to indicate each member of the tracer ensemble. Consecutive characters in a subscript indicate a second-order tensor, and a comma in the subscript indicates a partial derivative taken over the index following the comma.

Several improvements to the original inversion method presented in Bachman and Fox-Kemper (2013) were proposed in Bachman et al. (2015). These techniques are applied here to optimize the inversion method. Mathematical details are presented in Appendix A, but here it suffices to summarize the inversion problem as seeking the optimal solution for \mathbf{K} from the system of equations:

$$\frac{\lambda_{\mu}\overline{u_{i}'\tau_{\gamma}'} - \lambda_{\gamma}\overline{u_{i}'\tau_{\mu}'}(\bar{\tau}_{\mu,j})^{\dagger}\bar{\tau}_{\gamma,j}}{\lambda_{\mu} - \lambda_{\gamma}} = -K_{ij}\bar{\tau}_{\gamma,j} + \frac{\lambda_{\mu}\eta_{i\gamma} - \lambda_{\gamma}\eta_{i\mu}(\bar{\tau}_{\mu,j})^{\dagger}\bar{\tau}_{\gamma,j}}{\lambda_{\mu} - \lambda_{\gamma}}$$
(20)

$$\frac{\lambda_{\mu}\overline{u_{i}'\tau_{\gamma}'}(\bar{\tau}_{\gamma,j})^{\dagger}\bar{\tau}_{\mu,j} - \lambda_{\gamma}\overline{u_{i}'\tau_{\mu}'}}{\lambda_{\mu} - \lambda_{\gamma}} = -K_{ij}\bar{\tau}_{\mu,j} + \frac{\lambda_{\mu}\eta_{i\gamma}(\bar{\tau}_{\gamma,j})^{\dagger}\bar{\tau}_{\mu,j} - \lambda_{\gamma}\eta_{i\mu}}{\lambda_{\mu} - \lambda_{\gamma}}$$
(21)

$$\overline{u_i'\tau_\nu'} = -K_{ij}\bar{\tau}_{\nu,j} + \eta_{i\nu} \tag{22}$$

$$1 \le \gamma \le 3, \qquad 4 \le \mu \le 6, \qquad 7 \le \nu \le 9, \tag{23}$$

$$1 \le i \le 3, \qquad 1 \le j \le 3. \tag{24}$$

Equations (20)–(22) describe the inversion method we employ in this analysis, which is specific to the tracer configuration described in section 3.1. Subscripts (γ, μ, ν) indicate each of the three tracer sets, which are restored back to their initial profiles at a rate λ that is specific to each set and was previously specified following (18). The η terms represent uncertainty in the inversion, and the goal of the modified inversion

BACHMAN ET AL. 7 of 24

method (including the use of multiple tracers and extra sampling described below) is to make these terms as small as possible.

Following Bachman and Fox-Kemper (2013), the skill of the solution for \mathbf{K} is measured by reconstructing the eddy flux of *active* tracers that were withheld from the inversion method. Note that it is not at all obvious that the same \mathbf{K} would apply to passive and active tracers, so success by this metric implies a considerable simplification. Furthermore, in most coarse resolution ocean models, it is assumed that there is only one \mathbf{K} for all tracers, active and passive, so this diagnosis and evaluation technique is consistent with that approach. Previously this evaluation was done in idealized models that used potential temperature as the only active tracer variable. Here the global POP model uses both heat, θ , and salt, s, as state variables; therefore, we measure of the skill of the solution for \mathbf{K} via a cost function

$$C(i, \theta, s, \mathbf{K}) = \sqrt{\mathcal{E}_{i,\theta}^2 + \mathcal{E}_{i,s}^2},$$
 where (25)

$$\mathcal{E}_{i,\theta} = \frac{\left| \overline{u_i'\theta'} + K_{ij} \nabla_j \overline{\theta} \right|}{\left| \overline{u_i'\theta'} \right|} \quad \text{and} \quad \mathcal{E}_{i,s} = \frac{\left| \overline{u_i's'} + K_{ij} \nabla_j \overline{s} \right|}{\left| \overline{u_i's'} \right|}.$$
 (26)

The skill is thus an assessment of how well the flux-gradient hypothesis (4) is satisfied and is measured as the sum of squared relative errors in the reconstruction of both the heat and salt fluxes. Note that though the magnitudes of θ and s (and their respective eddy fluxes) may differ substantially from each other, the relative errors are normalized so that no reweighting is necessary. Also, since each component of the tracer flux vector is associated with only one row of \mathbf{K} , this minimization procedure can be done separately for each of the three flux directions i. Lastly, since the inversion method is local in space the procedure is repeated at each model grid point.

As suggested in Bachman et al. (2015), to minimize (25) one may sample different combinations of the nine tracer fields to best match the eddy fluxes of θ and s. As a 3 × 3 tensor, determination of $\mathbf K$ requires at least three tracers, but there is no guarantee that the optimal solution would require all nine tracers. To fully leverage this approach, every possible combination of 3, 4, ..., 8, and 9 tracers was used in a separate inversion, giving $\binom{9}{3} + \binom{9}{4} + ... + \binom{9}{9} = 466$ possible solutions to try in (25). Among these, the optimal solution is the one which minimizes (25). Recall that this optimization selects for the passive tracer combination that best predicts the active tracer transports, presumably because the local variations in this set of passive tracers statistically resemble the active tracers near this grid point.

Figure 1 shows a visual representation of this minimization process at the location 26° N, 30° W, and 230-m depth. Each solution for **K** is plotted according to its relative error in the heat and salt flux; the number of tracers used to calculate this solution are indicated by the color of the corresponding dot. The optimal solution (red diamond) is the solution that falls closest to the origin via the Euclidean distance metric, thus minimizing the cost function C. Here we also plot the solution using all nine tracers but without correcting for the tracer restoring (black diamond), which represents the "standard" solution method from Bachman and Fox-Kemper (2013) and the only analysis in Fox-Kemper et al. (2013).

The statistical improvement from using the optimization procedure is significant. For example, taking a global average of $\mathcal{E}_{1,\theta}$ at 230-m depth, the median relative error is 0.24 for the optimized solution (with 90th percentile at 1.09), and 1.06 for the standard solution (with 90th percentile at 7.37). The mean of $\mathcal{E}_{1,\theta}$ is 0.80 for the optimized solution and 10.46 for the standard solution, with standard deviations 14.80 and 277.38, respectively. Thus, at certain locations the standard inversion procedure can fail badly at reproducing the heat and salt fluxes with errors exceeding the fluxes, because at these locations some of the passive tracer fluxes are inconsistent with the active tracer fluxes in their relationship to their respective gradients. Alignment between multiple passive tracer gradients is one likely cause of this inconsistency, because alignment limits the accuracy of the tracer gradient pseudoinversions in (20) and (21). Another is spurious alignment of fluxes of tracers whose gradients are not aligned (recall that fluxes and gradients are just averages of instantaneous flow properties which retain considerable variability). However, sampling over all possible combinations of the tracers effectively finds which of the tracers collectively have the best correlation and optimizes the inversion by using only these.

BACHMAN ET AL. 8 of 24

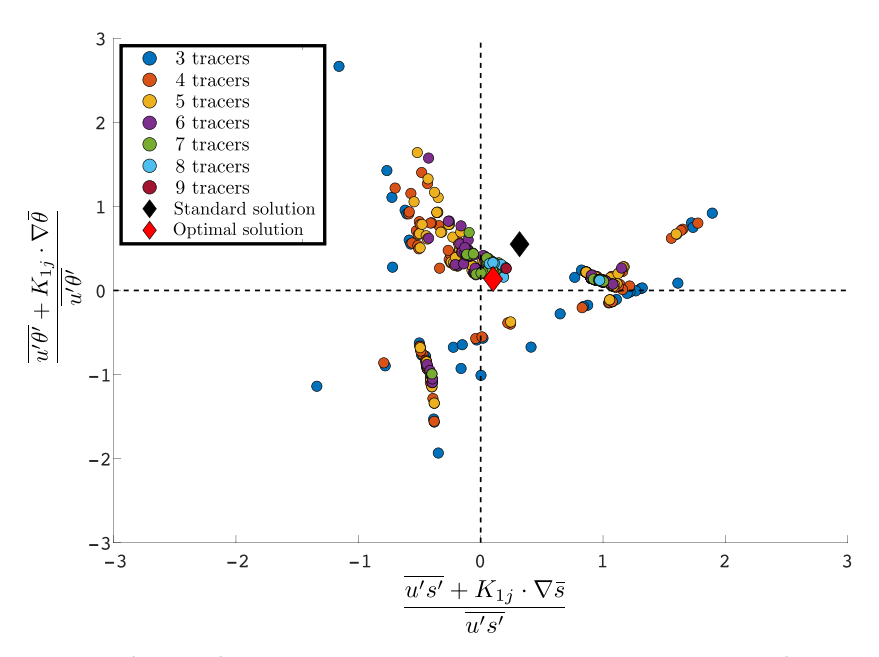


Figure 1. Visualization of the cost function minimization used to determine the optimal solution for K at 26°N, 30°W, and 230-m depth. Here all possible solutions obtained by inverting each combination of (up to) nine tracers are plotted as a function of its relative error in zonal heat and salinity flux. The optimal solution (red diamond) used six tracers and is the one which falls closest to the origin. The optimal solution shows a significant improvement over the solution to the standard inversion problem (A1) (black diamond).

3.3. Global Solutions

The optimized inversion method described in section 3.2 has been applied to the coarse-grained POP model output to produce maps of \mathbf{S}_H and its eigenvalues. The coarsened POP grid is approximately Cartesian, so that the tensor diagnosis measures correlations in the zonal, meridional, and vertical directions. Here we remind the reader that even though the focus is on the 2×2 tensor \mathbf{S}_H the inversion problem (20)–(22) is solved for the full 3×3 tensor \mathbf{K} . This 3-D inversion is necessary because vertical shearing and straining can have a significant effect on the lateral eddy transport (consider, e.g., the classic depiction of shear dispersion, cf. Taylor, 1953), which can only be properly captured by diagnosing the third column of \mathbf{S} . It is likely that in a 2-D inversion these effects would be aliased into the diagnosis of \mathbf{S}_H and result in a misleading solution.

By using the technique of iterating over all combinations of tracers, it is possible to select solutions for \mathbf{K} that satisfy certain criteria. For informing eddy parameterizations a sensible criterion is that the eigenvalues of \mathbf{S}_H must be positive, indicating downgradient diffusion. Though positive eigenvalues are not necessarily mandatory from the physical perspective of what eddies may do in a limited region, it is likely that they are necessary for the GM-Redi scheme to be numerically stable. We proceed to visually compare the elements of \mathbf{K} and their skill at reproducing the eddy heat fluxes from (a) the standard inversion technique (A1), (b) the optimized technique in section 3.2, and (c) the optimized technique including only solutions with positive eigenvalues of \mathbf{S}_H .

Figures 2–4 show global maps of the horizontal (upper left 2×2) subtensor of **K** taken at z=230-m depth. The optimized inversion is shown first in Figure 2. The tensor elements take both positive and negative signs, with the negative values on the diagonal elements K_{11} and K_{22} showing a slight tendency to occur in the energetic regions in the Southern Ocean, western boundary currents, and along the equator. Negative values are also significantly more common in the off-diagonal elements, where they are not prohibited (as they may reflect only a rotation of the principal axes and not a negative eigenvalue). The global mean absolute value for each element is 7.06×10^3 m²/s for K_{11} , 2.45×10^3 m²/s for K_{12} , 4.34×10^3 m²/s for K_{21} , and 2.26×10^3 m²/s for K_{22} . These values are significantly larger than are typically used for eddy-free global ocean modeling (e.g., Danabasoglu & Marshall, 2007) but are appropriate for the 2° grid scale of the coarse-grained output used here. For example, a dimensional scaling of these values using a midlatitude grid length scale of 1×10^5 m for the 2° grid implies eddy time scales ranging from 0.5 to 2 months. Note that the timescales implied here are decorrelation timescales and not the eddy lifetime, which are significantly longer and can range into several

BACHMAN ET AL. 9 of 24

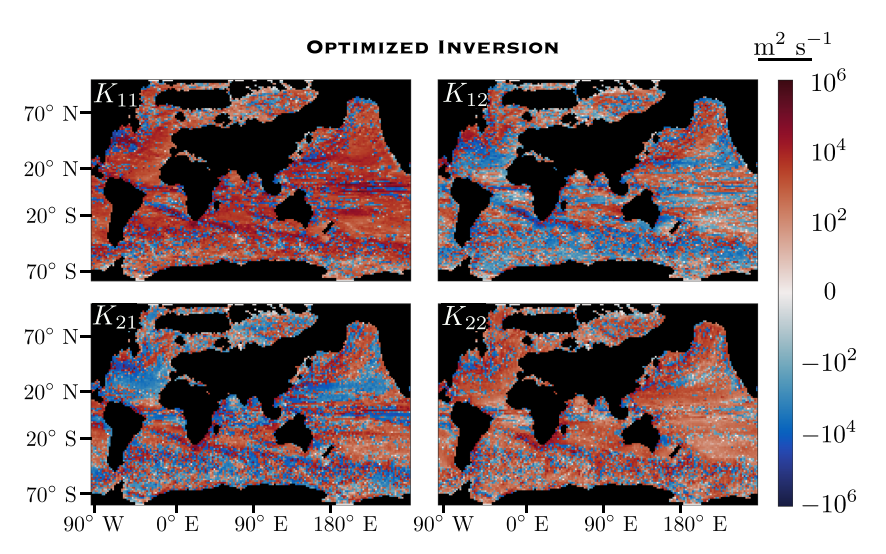


Figure 2. Global map of the horizontal elements of **K** obtained from the optimized inversion method (section 3.2) at z = 230 m.

months (Chelton et al., 2011). The elevated values for K_{11} compared with the others hint at anisotropy that tends to align the major axis of \mathbf{S}_H with the zonal direction, which will be explored further in section 4.

The tensor elements diagnosed using the standard inversion (A1) are shown in Figure 3. Visual comparison against Figure 2 shows overall a similar spatial distribution of diffusivity values between the two methods. The most obvious difference is that the optimized inversion shows significantly more (strongly) negative values for K_{11} that tend to occur in the energetic regions listed above. Similarly, K_{22} shows a clustering of negative values along the equator in the Indian and western Pacific Oceans. It is unclear why negative diffusivities tend to occur in these regions. More generally, comparing these Figures shows the utility of the optimized method in detecting antidiffusive behavior in θ and s. The standard inversion uses all nine tracers, several of which undergo atypical behavior and thus collectively do not reproduce the heat and salt fluxes well.

Figure 4 again shows the global maps using the optimized inversion, but with the restriction that only solutions with positive eigenvalues for \mathbf{S}_H are kept when iterating over all the tracer combinations. The effects of this restriction are clear in the maps of K_{11} and K_{22} , which have only positive values (it can be shown that this must be the case using the well-known theorems that the determinant of \mathbf{S}_H is the product of its eigenvalues and the trace of \mathbf{S}_H is the sum of its eigenvalues). White regions indicate where there is no solution

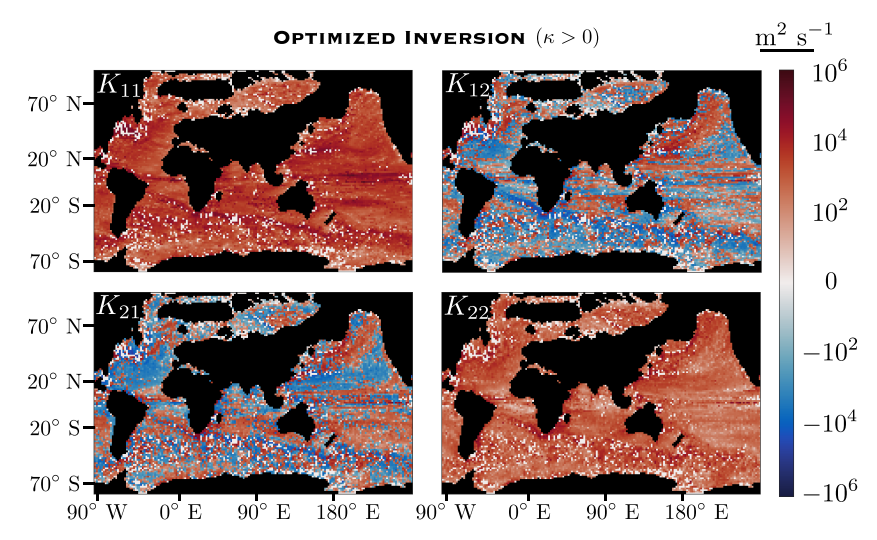


Figure 3. Global map of the horizontal elements of **K** obtained from the standard inversion method (A1) at z = 230 m.

BACHMAN ET AL. 10 of 24

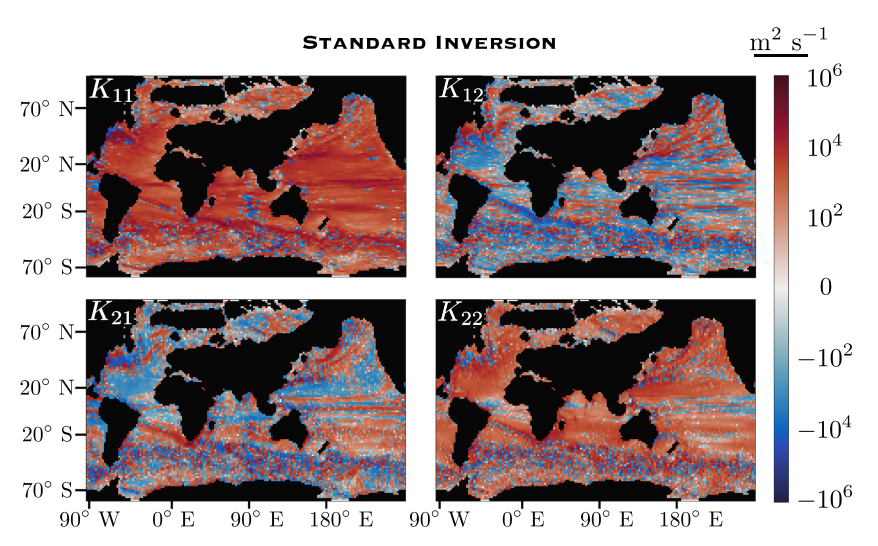


Figure 4. Global map of the horizontal elements of **K** obtained from the optimized inversion method when it is restricted to only include solutions with positive eigenvalues of S_H . Diagnostics are taken at z = 230 m.

that obeys this restriction, meaning that diffusion is upgradient along at least one of the principal axes in all of the diagnosed tracer combinations. Aside from the locations with no solution the maps of the off-diagonal elements are again qualitatively similar to those in Figures 2 and 3.

Akin to the cost function defined in (25), the solutions can be used to reconstruct the eddy fluxes of tracers that were withheld from the diagnosis. The relative errors of the reconstructed fluxes can then be used to assess the improvement gained by using the optimized inversion technique versus the standard technique or the degradation that results from restricting the solution to include only positive eigenvalues. Figure 5 shows global maps of the reconstructed lateral eddy heat fluxes at z=45 m in comparison with those diagnosed from the simulation (top row). The reconstructions using the optimized inversion are shown in the second row, the standard inversion in the third row, and the version with positive eigenvalues in the bottom row. The z=45-m level is chosen for this comparison instead of the previously used z=230-m level because its proximity to the surface results in greater variability in the fluxes and thus provides clearer visual evidence of the differences between the three types of reconstruction.

The visual agreement between the diagnosed heat fluxes and those from the optimized inversion is nearly perfect, except for small differences that are only apparent at the level of individual grid cells. The only feature where a more significant difference appears is in the positive heat flux in the central Pacific Ocean just south of the equator, for which the diagnosed values extend further eastward. The standard inversion also shows strong agreement with the diagnosis, but the differences appear in larger features. There is again a noticeable difference in the structures in the equatorial Pacific, though this includes the negative heat flux region north of the equator as well. The equatorial Indian ocean shows a tendency toward negative values in the inversion, as opposed to generally positive values in the diagnosis. The largest differences occur along the pathway of the Antarctic Circumpolar Current (ACC), where in the diagnosis there is a distinct band of positive zonal heat fluxes extending eastward off of southern Africa tapering into a weaker band of fluxes around the rest of the Southern Ocean. The band appears shorter in the standard inversion, but the fluxes throughout the rest of the Southern Ocean are significantly stronger and do not match well with the diagnosis at all. The inversion with positive eigenvalues broadly agrees with the optimized inversion but lacks skill in reproducing smaller details. The most noteworthy lack of skill appears in the Gulf Stream region, which appears less organized and more noisy in comparison with the diagnosis, perhaps a consequence of the difficulty in achieving a clean scale separation in this region (Grooms et al., 2011).

The global mean relative errors between the diagnosis and optimized inversion are 0.80 and 1.07 for the zonal and meridional fluxes, respectively, though these values are skewed higher due to individual locations where the reconstructions are very poor. The median relative errors are 0.24 and 0.23, with the 80th percentile at 0.73 and 0.72, respectively. These skill metrics are significantly improved over the standard inversion, for which the mean relative errors are 10.45 and 16.55, the median relative errors are 1.06 and 0.91, and the

BACHMAN ET AL. 11 of 24

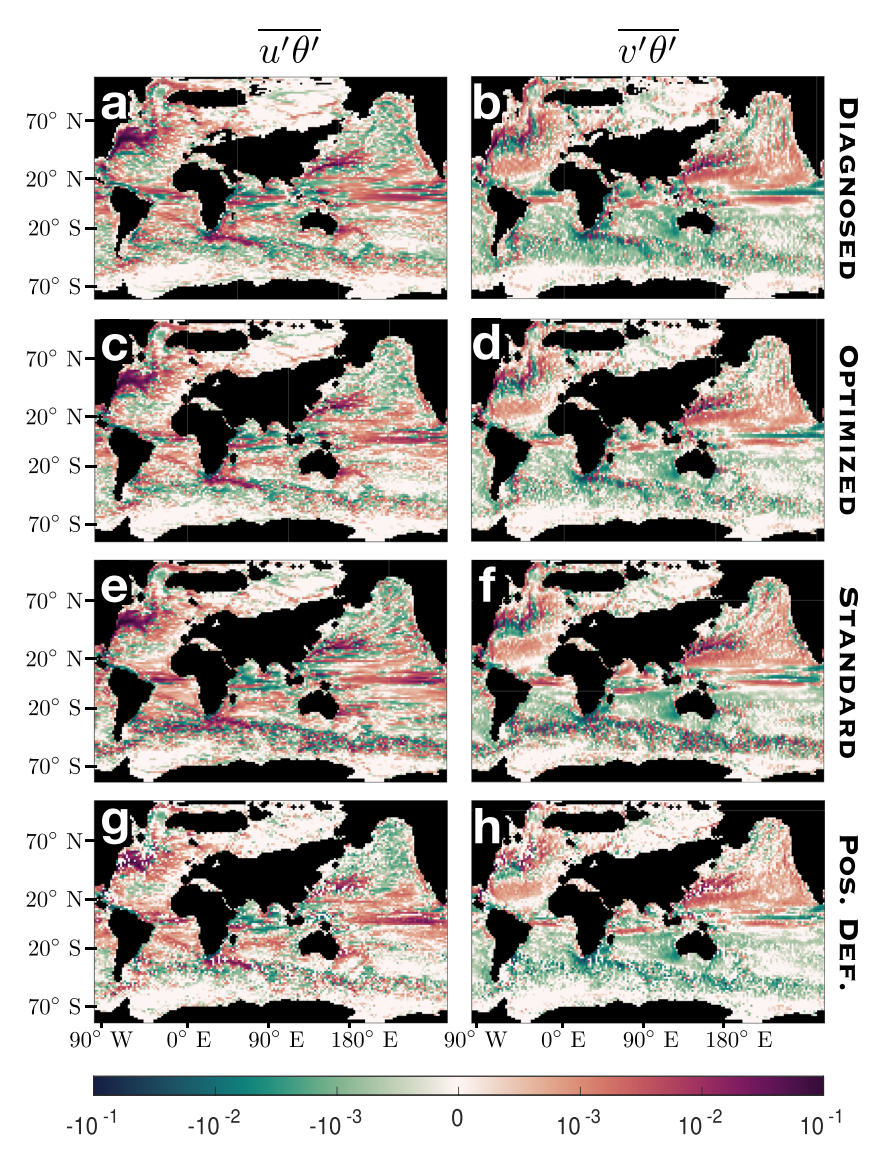


Figure 5. Eddy heat fluxes from the model diagnosis (a, b), compared against reconstructions using the optimized inversion (c, d), standard inversion (e, f), and optimized inversion restricted to positive definite eigenvalues for S_H (g, h). In panels (g) and (h) locations that have no solution are filled in with zeros. All maps are shown at z = 45 m.

80th percentiles are at 3.47 and 2.74. The skill from using positive definite eigenvalues falls in between, with mean relative errors 6.99 and 2.00, median relative errors 0.71 and 0.67, and 80th percentiles 1.34 and 1.19.

These results confirm that, to the extent that the flux-gradient relationship (4) is appropriate, passive tracers and the thermodynamic variables experience mostly positive diffusion by the eddies over most of the world ocean. Antidiffusion does occur but not necessarily for all tracers at a given location. The skill of the inversion technique diminishes when antidiffusion occurs on the withheld active tracer but not on the sampled passive tracers. For the sake of informing parameterizations we recommend using only results from the optimized inversion with positive-definite symmetric eigenvalues, as it is unlikely that employing an antidiffusive parameterization would be robustly stable in practice.

4. Eigenvalues, Eigenvectors, and Anisotropy of S_H

We now proceed to examine the eigendecomposition of \mathbf{S}_H with the intent of building a framework for applying an anisotropic GM-Redi parameterization. Given a suitable expression for the scalar GM coefficient, four ingredients are necessary for building this framework: (1) the ratio of the eigenvalues of \mathbf{S}_H , (2) the

BACHMAN ET AL. 12 of 24

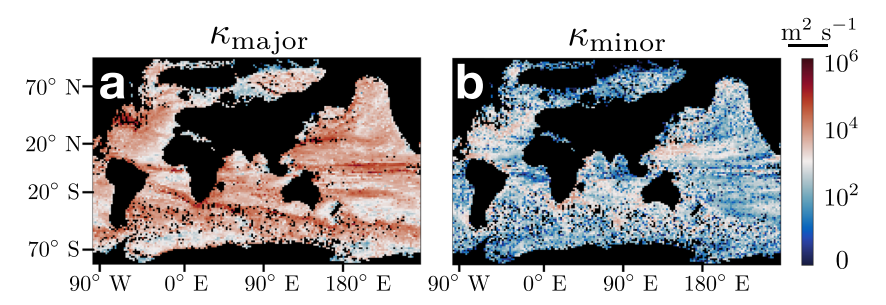


Figure 6. Global maps of the (a) major and (b) minor eigenvalues of S_H at z=230 m.

orientation of its eigenvectors, (3) a relationship between the the 2×2 tensors S_H and S_H^* in S and A, respectively, and (4) a scaling for at least one of the eigenvalues. For isotropic transport the third requirement is equivalent to needing a relationship between the GM and Redi coefficients, but since the focus here is on anisotropic transport, we keep the relationship in tensor form for generality. We proceed to address each of these four ingredients one at a time.

4.1. Ratio of Eigenvalues

Given S_H with positive eigenvalues, a diagnosis of the ratio between its major and minor eigenvalues, r, is straightforward. Maps of these eigenvalues are shown in Figure 6. The major eigenvalues tend to be larger in areas with strong eddy kinetic energy (Von Storch et al., 2012) such as western boundary currents, the ACC, and the equatorial latitudes. The minor eigenvalues show some enhancement in these same regions, but this is not as pronounced as for the major eigenvalue.

The ratio of the eigenvalues exhibit a large amount of variability, but its spatial distribution is noisy and does not correlate well with any of the mean fields (not shown). Figure 7a shows a histogram of r at z=230 m partitioned into 100 discrete bins between 1 and 50 and indicates that r tends toward smaller values but has has a nonnegligible probability of taking values even beyond the bin limit of 50. The histogram values have

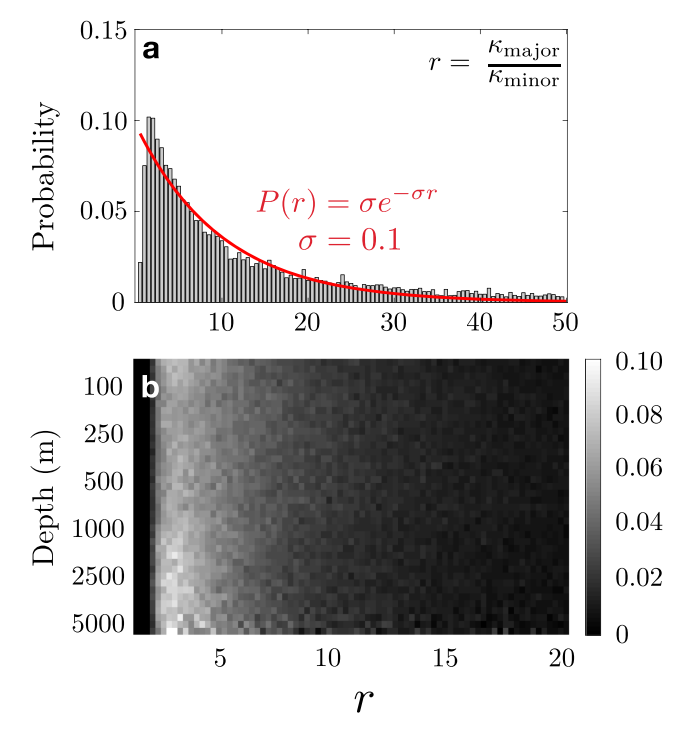


Figure 7. (a) Discrete probability distribution of the ratio of eigenvalues at z = 230 m, along with the best fit exponential distribution curve (red line). (b) Intensity plot showing the probability distribution of the eigenvalue ratio as a function of depth.

BACHMAN ET AL. 13 of 24

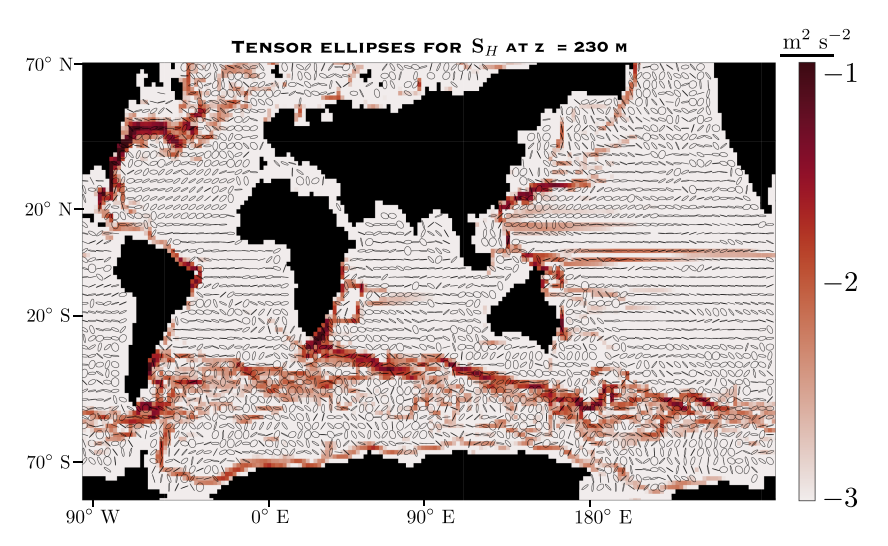


Figure 8. Tensor ellipses for S_H taken at z = 230 m, overlaid on a color plot of the Base-10 logarithm of mean kinetic energy. The length of the major axis of each ellipse is set to be two grid cells wide, and the eccentricity is set by the ratio between the logarithms of each eigenvalue (a larger ratio implies higher eccentricity).

been normalized so that the cumulative area of the bars is 1, which allows us to fit a continuous probability density function (PDF) to the histogram. A reasonable approximation is obtained using an exponential distribution, $P(r) = \sigma e^{-\sigma r}$, with $\sigma = 0.1$ (red line).

The PDFs tend to be similar at all depths (Figure 7b). The center of mass of the PDFs over all depths is calculated as

$$\langle r \rangle = \sum_{i=1}^{n} r_i p_i, \tag{27}$$

where i is the bin number and p is the probability within that bin. For the PDFs binned from 1 to 50 $\langle r \rangle$ is 12.37; if the bins are restricted from 1 to 20 to eliminate outliers and extremely large values, $\langle r \rangle$ is reduced to 7.22. Assuming one of the eigenvalues is known, a very basic approach for constructing a parameterization would be to take a constant value for $\langle r \rangle$ and apply it as a rule for scaling the other eigenvalue. A slightly more advanced option would be to sample $\langle r \rangle$ from an exponential PDF with $\sigma=0.1$, which effectively adds a stochastic element to the anisotropic GM-Redi closure.

4.2. Orientation of Eigenvectors

The second ingredient needed to build an anisotropic GM-Redi parameterization is knowledge of how the eigenvectors of \mathbf{S}_H are oriented. Because the eigenvectors of a symmetric matrix are orthogonal with respect to one another, it is sufficient to characterize only one of them; assuming both eigenvalues are known, the direction of the other eigenvector can be obtained by solving the homogeneous matrix equation $(\mathbf{S}_H - \kappa \mathbf{I}) \cdot \mathbf{v} = \mathbf{0}_{2\times 1}$ using the remaining eigenvalue.

The eigenvalues and eigenvectors together can be visually represented using tensor ellipses, where the major axis of the ellipse is directed along the major principal axis of the tensor and the eccentricity of the ellipse is determined by the ratio between the major and minor eigenvalues. Figure 8 shows a global map of the tensor ellipses for \mathbf{S}_H taken at z=230 m, overlaid on a color plot of the Base-10 logarithm of mean kinetic energy. For ease of visualization the eccentricity of each ellipse is determined by the ratio of the *logarithms* of each eigenvalue rather than their raw values (otherwise nearly all of the ellipses would be so eccentric as to appear as straight lines). Also, the major axis of each ellipse is constrained to be two grid cells wide, so locations with high eccentricity tend to appear as lines that lie parallel to the major eigenvector direction. From a global perspective there is considerable variability among the ellipse shapes and directions. However, close inspection hints at a general tendency for more eccentricity in regions of high kinetic energy, with the major eigenvector tending to be oriented in the along-stream direction. The aim of this section is to explore possible causes for the eigenvectors to be oriented in this way and to assess how this behavior might be quantified for the sake of building a parameterization.

BACHMAN ET AL. 14 of 24

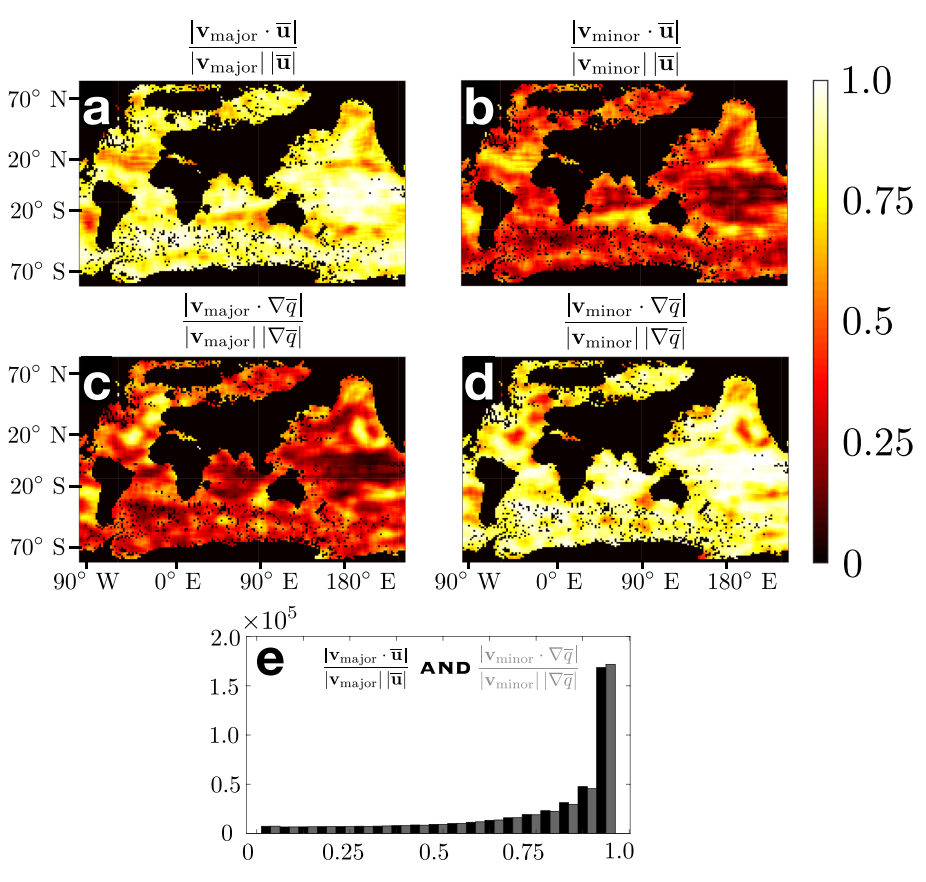


Figure 9. Global maps of the cosine of the angle between the (a) major principal axis and mean flow vector, (b) minor principal axis and mean flow vector, (c) major principal axis and Ertel potential vorticity gradient, and (d) minor principal axis and Ertel potential vorticity gradient, all at z = 230 m. (e) Histograms corresponding to panels (a, black) and (d, gray).

Various mechanisms have been studied for their role in suppressing eddy diffusivity, such as jets (Ferrari & Nikurashin, 2010; Klocker et al., 2012), PV gradients (Srinivasan & Young, 2014), and topographic gradients (Isachsen, 2011), or directionally enhancing it, such as shear dispersion (Smith, 2005; Young et al., 1982). These mechanisms have been explored in the POP simulations by projecting the eigenvectors of \mathbf{S}_H into the bottom topographic gradient, $\nabla \bar{H}$, barotropic PV gradient, $\nabla (f/H)$, Ertel PV gradient, $\nabla \bar{q}$, and mean flow vector, $\overline{\mathbf{u}}$. The latter is used to examine both jet suppression and shear dispersion, as both mechanisms essentially act to enhance the along-stream diffusivity relative to the cross-stream diffusivity.

The topographic and barotropic PV gradients showed no systematic correlation with either of the eigenvector directions and are not shown here. Figure 9 shows the projections of the eigenvectors, v, onto both the mean flow vector (panels a and b) and Ertel PV gradient (panels c and d). The projections are normalized to display the absolute value of the cosine of the angle formed between the two vectors. The absolute value is used because the eigenvectors are only unique up to multiplication by a scalar, meaning that if v is an eigenvector, then so is $-\mathbf{v}$. Values near one (lighter colors) thus represent very close alignment between the vectors, while values near 0 (darker colors) indicate that the vectors are nearly orthogonal. The lighter shades in panels (a) and (d) show generally good agreement globally between the major principal axis and the mean flow vector, or the minor principal axis and the PV gradient, respectively. Recall that the eigenvectors must be perpendicular, so this is also implies that the epineutral PV gradient and mean flow direction tend to be perpendicular. The spatial patterns are quite similar: Both projections tend to have uniformly high values except in conspicuous patches, such as in the North Atlantic Gyre, across the southern Indian Ocean, a band immediately south of the Pacific Cold Tongue, and other smaller regions. Patches of very large (nearly white) values occur in the equatorial latitudes in all ocean basins, as well as in the South Atlantic Ocean along the path of the ACC. Locations of obviously weak alignment between the minor principal axis and the PV gradient in panel (d) are seen in the eastern Atlantic and Pacific Oceans and are organized into patches

BACHMAN ET AL. 15 of 24



instead of broad, diffuse regions as in panel (a). Several measures of the resolved flow (i.e., dimensionless parameters, kinetic energy, and enstrophy) were examined to try to understand whether these patterns had any kind of spatial correlation, but no conclusive results were found.

Histograms showing the number of occurrences for each value in panels (a) and (d) are shown in Figure 9e, with the histogram for panel (a) shown by the black bars for panel (d) by gray bars. Both histograms are formed using values taken over all depths and are nearly identical to each other, with the large majority of occurrences in the bin spanning 0.9 and 1.0. These results suggest that anisotropic diffusion might be due to both large-scale shear dispersion and PV gradient barriers, depending on location. It should be noted that both effects may be present in the same flow structure; for example, a zonal jet U may induce shear dispersion in the along-stream direction concurrently with a PV gradient in the cross-stream direction associated with its second derivative, $\partial_{vv}U$.

With regard to building an anisotropic GM-Redi closure based on either the mean flow vector or the PV gradient, we will proceed by using the PV gradient as the primary guide for the minor principal axis. Initial experimentation with prognostic simulations using anisotropic GM/Redi showed that further refinement is likely to be needed, as both mean flow and PV gradients had undesirable effects in some regions and feedbacks need to be considered.

4.3. Relating Diffusive and Advective Transport Coefficients Through Vertical Structures

Scalings for the isoneutral diffusivity have generally been more difficult to pursue than for the GM transport. Because GM is designed to mimic to the phenomenology of baroclinic mesoscale eddies, previous authors have justified scalings based on (for example) the rate of potential energy extraction (Fox-Kemper et al., 2008), the estimated width of baroclinic zones (Green, 1970), and the overall eddy energy density (Marshall et al., 2012). The diffusive Redi transport, in essence, is one step removed from this phenomenology; it is not associated with potential energy extraction or restratification, but it represents the same eddy field as does GM and thus may be expected to exhibit similar dependence on the shear, stratification, and energetics.

Indeed, previous studies have derived relationships between the GM and Redi coefficients that suggest a key difference lies in their vertical structures (Smith & Marshall, 2009). Stochastic theory predicts that $\mathbf{S}_H = \mathbf{S}_H^*$, but only within an isopycnal layer where the diffusivity has no vertical dependence (Dukowicz & Smith, 1997; Smith, 1999). The form of GM that arises from the stochastic theory differs from that recommended by Gent et al. (1995), where the difference lies in the placement of a vertical derivative operator (Smith & Gent, 2004). The Gent et al. (1995) version is preferred in modern ocean models because it cleanly reduces to the antisymmetric tensor form shown in (11), is more amenable to numerical implementation, and is consistent in extracting resolved potential energy. Nonetheless, both forms of GM agree that \mathbf{S}_H and \mathbf{S}_H^* are the same tensor and differ only in their vertical structures.

If one takes the stochastic theory derived by Dukowicz & Smith (1997, Equation 42) but instead substitutes the Gent et al. (1995) parameterization for the eddy-induced velocity, the relationship between the vertical structures of $\bf S$ and $\bf S_H$ becomes

$$\mathbf{S}_{H} \cdot \partial_{z} \mathbf{L} = \partial_{z} \left(\mathbf{S}_{H}^{*} \cdot \mathbf{L} \right). \tag{28}$$

We may now left multiply (28) by a rotation matrix \mathbf{R}_2 to rotate the horizontal coordinates into alignment with the principal axes of \mathbf{S}_H , such that

$$\mathbf{R}_{2} \cdot \left(\mathbf{S}_{H} \cdot \partial_{z} \mathbf{L} \right) = \mathbf{R}_{2} \cdot \partial_{z} \left(\mathbf{S}_{H}^{*} \cdot \mathbf{L} \right). \tag{29}$$

Because matrix multiplication is associative, the parentheses on the left may be moved to bracket the product of the rotation matrix and \mathbf{S}_H , which due to the coordinate rotation is simply the diagonal matrix of eigenvalues. The multiplication on the right proceeds in the same way, except that an extra term is introduced to bring the rotation matrix inside the vertical derivative. Then (29) can now be expressed as

$$\kappa_{i} \partial_{z} L_{i} = \partial_{z} \left(\kappa_{i}^{*} L_{i} \right) - \left[\partial_{z} \mathbf{R}_{2} \cdot \left(\mathbf{S}_{H}^{*} \cdot \mathbf{L} \right) \right]_{i}, \tag{30}$$

where κ_i and κ_i^* are the eigenvalues of \mathbf{S}_H and \mathbf{S}_H^* , respectively, and $i = \{1, 2\}$ (no summation on repeated indices is implied in this case). The first term on the right can be expanded using the product rule, and after

BACHMAN ET AL. 16 of 24

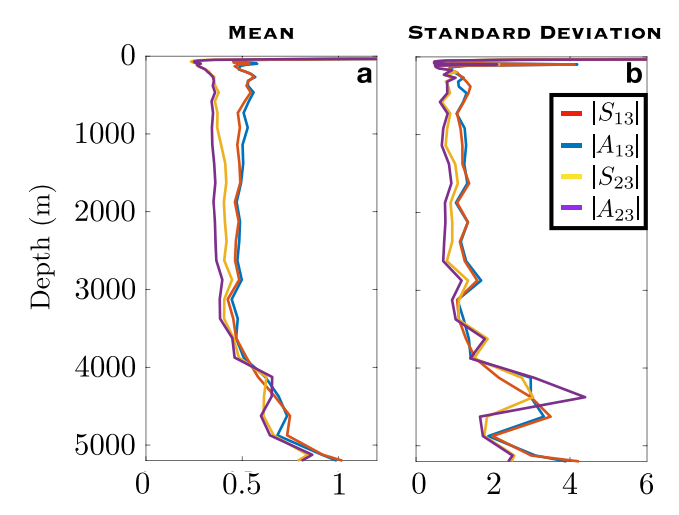


Figure 10. Vertical structures of the (a) mean and (b) standard deviations of S_{13} , A_{13} , S_{23} , and A_{23} . Note that the horizontal axes in these plots are not normalized.

straightforward algebra yields

$$\kappa_{i} = \kappa_{i}^{*} + \left(\frac{L_{i} \partial_{z} \kappa_{i}^{*}}{\partial_{z} L_{i}} - \frac{\left[\partial_{z} \mathbf{R}_{2} \cdot \left(\mathbf{S}_{H}^{*} \cdot \mathbf{L}\right)\right]_{i}}{\partial_{z} L_{i}}\right). \tag{31}$$

At any vertical level the eigenvalues for S_H and S_H^* thus differ by the quantity in the parentheses, whose magnitude depends on how quickly the diffusivity, isopycnal slope, and eigenvector directions vary with z. Given a suitable scaling for each κ_i^* (the GM coefficients in the principal axes coordinate system), it is thus possible to directly calculate the corresponding Redi coefficients, κ_i . However, the robustness of this calculation would likely be dubious due to the presence of the slope derivative in the denominator of (31) and possibly would return negative values for κ_i if no constraints on the calculation were enforced. Equation (31) thus provides a new, explicit relationship between the eigenvalues of the GM and Redi tensors but may not be a very useful tool for building a parameterization.

Because the difference between the GM and Redi eigenvalues is determined by the term in parentheses, a next logical step is to determine its magnitude relative to the eigenvalues themselves. The purpose of this approach is to quantify the terms in parentheses and determine whether it is justified to ignore them and use the common approach of setting the GM and Redi coefficients equal to each other. A key complication is that diagnosis of \mathbf{S}_H^* or κ_i^* is not possible using the tracer inversion method—by (11) the inversion method can diagnose \mathbf{A} , but all instances of \mathbf{S}_H^* inside of \mathbf{A} are dotted with the isopycnal slope. It is thus not possible to untangle the tensor from the slope and diagnose its elements or eigenvalues. We instead compare each element of $\mathbf{S}_H \cdot \mathbf{L}$ and $\mathbf{S}_H^* \cdot \mathbf{L}$, keeping in mind that if these elements are similar at all depths then so must be the eigenvalues.

Figure (10) shows vertical structures of S_{13} , S_{23} , A_{13} , and A_{23} , which by (10) and (11) correspond to the individual elements of $\mathbf{S}_H \cdot \mathbf{L}$ and $\mathbf{S}_H^* \cdot \mathbf{L}$. The absolute value of each element is used to properly compare them against each other, since each element can take positive or negative values. Each line in the plot represents a global average of the corresponding element. There is extremely close agreement in both (a) the mean and (b) the standard deviation of each element pair (S_{13} vs. A_{13} , and S_{23} vs. A_{23}). The vertically averaged relative error between S_{13} and S_{13} is 3.6% for the mean value and 6.8% for the standard deviation, and is 7.3% for the mean and 12.5% for the standard deviation between S_{23} and S_{23} . The standard deviations are several times larger than the means, reflecting variability in the eddy diffusivity at different spatial locations.

A second way of comparing these elements is to produce vertical profiles of their ratio. Figure 11a shows globally averaged profiles of $|S_{13}| \left(|S_{13}| + |A_{13}| \right)^{-1}$ and $|S_{23}| \left(|S_{23}| + |A_{23}| \right)^{-1}$, where the denominators are chosen in this way so that there is no risk of dividing by 0. Good agreement between the elements should make these expressions tend toward 0.5, while poor agreement should make them tend toward either 1.0 if S >> A or zero if A >> S. The mean values (solid lines) tend to remain near 0.5 at all depths, with the

BACHMAN ET AL. 17 of 24

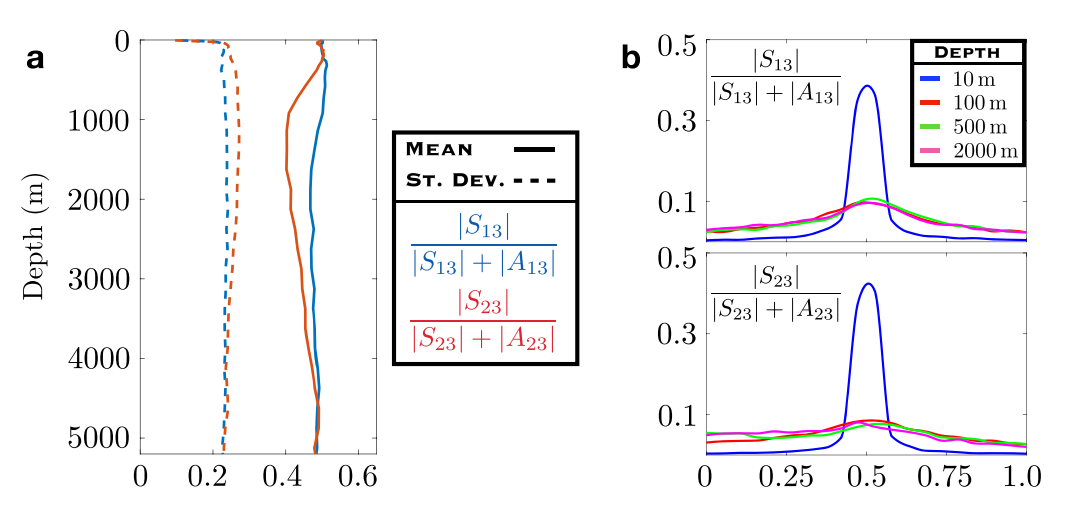


Figure 11. (a) Vertical structures of the ratio between the magnitude of *S* elements and *A* elements. Similar values between these elements imply that the mean (solid lines) will be near 0.5. (b) Probability density functions of these ratios taken at different depths.

greatest difference (-0.09) occurring for the S_{23} function at around 1,000-m depth. The standard deviations for both functions are around 0.25, which may be partly due to spatial variability in the eddy diffusivity as well as to errors in the inversion method (the magnitude of the elements in the third rows and columns of \mathbf{K} is expected to be about a factor of 1,000 smaller than those in \mathbf{S}_H , and are thus more prone to uncertainty in the estimate).

The vertical structure functions in Figures 10 and 11a are calculated by averaging each quantity globally, which can potentially mask significant local variability. To assess the variability of these functions, PDFs of $|S_{13}| \left(|S_{13}| + |A_{13}| \right)^{-1}$ and $|S_{23}| \left(|S_{23}| + |A_{23}| \right)^{-1}$ are calculated at different depths and shown in Figure 11b. The PDFs are calculated by taking all values of each variable at a given depth, binning them into 20 equally spaced bins between 0 and 1, and calculating the probability that the value falls within each bin. Both variables exhibit similar behavior. There is a strong tendency near the surface for both variables to fall within the bins near 0.5, indicating a tendency for the **S** and **A** elements to be of very similar magnitude. This tendency rapidly decays with depth, and below 100 m the variables show a weaker preference to fall within the bins near 0.5. All distributions are essentially symmetric about 0.5 and are approximately Gaussian. These results are consistent with those in panel (a), where the mean values remain very close to 0.5 but have nonnegligible standard deviations (\sim 0.2) at almost all depths, except for a very thin layer near the surface where the standard deviation decreases sharply.

The standard deviations in Figure 11a and the PDFs in Figure 11b indicate some variability in the relative magnitudes and vertical structures of \mathbf{S}_H and \mathbf{S}_H^* , which may either be locally significant deviations between these quantities or diagnostic uncertainty. The approximately Gaussian structure of the PDFs, along with the standard deviations near 0.2 at most depths, suggests that around 2/3 of the values for the GM and Redi coefficients are within a factor of 2 of each other. Based on these results, in many instances it is appropriate to make the approximation $\mathbf{S}_H = \mathbf{S}_H^*$, which greatly simplifies the tensorial form of the flux-gradient relationshop (Griffies, 1998). Note that this diagnostic approach *includes* contributions from the terms in parentheses in (31), so this agreement demonstrates that they are not large in comparison to the eigenvalues in most circumstances (although exceptions exist, which are represented by the tails of the PDFs in Figure 11b). To accommodate these results in a parameterization a prudent approach would be to set the GM and Redi coefficients equal to each other and then (optionally) perturb one by less than a factor of 2 or so, if desired.

4.4. Eigenvalue Scaling

Stochastic theory (Dukowicz & Smith, 1997) predicts that the GM and Redi tensors are identical in orientation, and the key result from the previous subsection is that these tensors are very similar in magnitude to each other at all depths. This similarity raises the possibility that one could use extant scalings for the GM thickness diffusivity to then scale the Redi diffusivity, or equivalently, the eigenvalues of \mathbf{S}_H . This would be especially useful because scalings for the Redi diffusivity are more difficult to justify based on kinematic

BACHMAN ET AL. 18 of 24

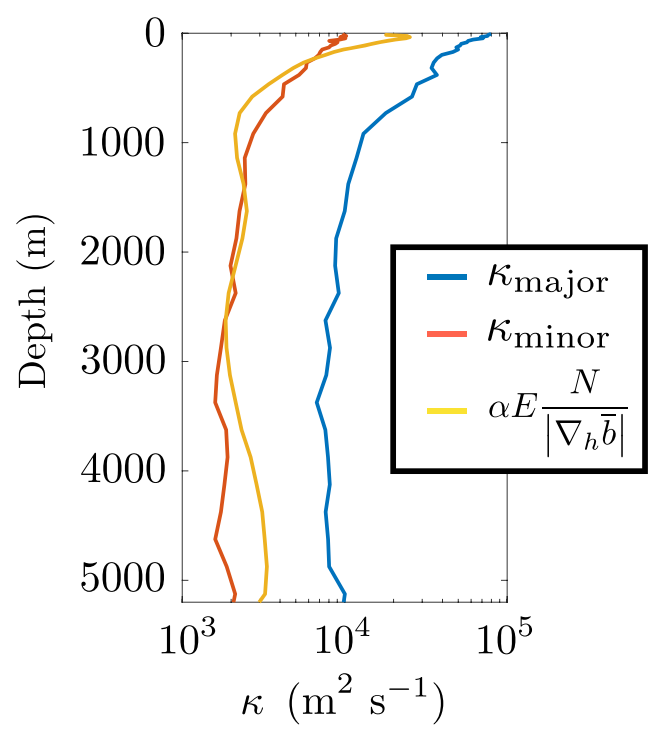


Figure 12. Global mean vertical structures of the major (blue line) and minor (red line) eigenvalues of S_H , compared against the vertical structure of the GEOMETRIC GM coefficient (gold line).

arguments than are those for GM. It would also represent the final piece of a potential anisotropic parameterization, which would be to scale one of the eigenvalues of \mathbf{S}_H and then use the anisotropy ratio in section 4.1 to determine the other.

The goal of this analysis is not to test different diffusivity scalings, as previous studies have done (e.g., Bachman et al., 2017; Eden et al., 2009). Rather, the goal here will be to use a single, skillful scaling for the GM coefficient and examine whether it is a good approximation to one of the eigenvalues of \mathbf{S}_H . The scaling we choose is the GEOMETRIC GM coefficient (Marshall et al., 2012; Mak et al., 2017), whose functional form is

$$\kappa_{GEOM} = \alpha E \frac{N}{\left| \nabla_h \bar{b} \right|},\tag{32}$$

where E is the total eddy energy, N is the Brünt-Vaisala frequency, and α is a nondimensional efficiency parameter bounded in magnitude by one. The analysis here uses a constant $\alpha = 0.2$, which is similar to that diagnosed by Marshall et al. (2012) and Bachman et al. (2017).

Figure 12 compares the globally averaged vertical structures of the major (blue line) and minor (red line) eigenvalues of \mathbf{S}_H against that of κ_{GEOM} (gold line). The vertical structures of κ_{GEOM} and the minor eigenvalue are similar in magnitude across all depths, with a depth mean relative error between them of 23.8% and diffusivities ranging from approximately 10^3 m²/s in the abyssal ocean to 10^4 m²/s at the surface. In contrast, the major eigenvalue tends to remain a full order of magnitude larger at all depths. Both eigenvalues have very similar vertical structures. It is possible that the fit of κ_{GEOM} to the minor eigenvalue could be improved by a more sophisticated diagnosis of the scaling coefficient α , but the model diagnostics needed for direct calculation of α were not available. If the GEOMETRIC scheme is a good predictor of the isotropic diffusivity, then this comparison also suggests that horizontal anisotropy might be stronger due to mechanisms that enhance one eigenvalue (e.g., shear dispersion) rather than those that suppress one (e.g., topography or PV barriers).

4.5. A Provisional Recipe for Anisotropic GM-Redi

Assembling all of the results from sections 4.1 to 4.4 allows us to construct a recipe for an anisotropic GM-Redi closure. Here this recipe will make use of κ_{GEOM} as the recommended GM thickness diffusivity

BACHMAN ET AL. 19 of 24



for the minor eigenvalue, though not all ocean circulation models may have the subroutines required for its implementation (i.e., a skillful prognosis or budget for the eddy energy). Modelers who wish to use an alternative formulation for the GM coefficient may substitute it into this recipe without needing to adjust the other parts.

The recipe begins with κ_{GEOM} , which will be used as the minor eigenvalue of both \mathbf{S}_H and \mathbf{S}_H^* . The anisotropy ratio r is found by sampling from the exponential distribution $P(r) = \sigma e^{-\sigma r}$ with $\sigma = 0.1$, and the major eigenvalue is set by multiplying κ_{GEOM} by this sample. The direction of the minor eigenvector is down the local PV gradient.

Note that there will be shear dispersion in the model calling such a parameterization, providing anisotropic effective diffusion even if r = 1 is used. The analysis here is based on diagnosing the *total* anisotropic diffusion from the POP2 simulation, so care needs to be taken to avoid double counting of anisotropy in the parameterization and in the resolved shear dispersion of the calling model.

It is not necessary to explicitly find the direction of the major eigenvector because both eigenvalues are nonnegative and are guaranteed to remain nonnegative under any continuous coordinate transformation. That is, since the minor eigenvector is known then the angles it forms with both grid ordinates are known, and one may simply rotate the diagonal matrix of eigenvalues into whichever ordinate is most convenient and the eigenvalues will still be nonnegative. The resulting \mathbf{S}_H is thus guaranteed to represent diffusive behavior no matter which way the tensor is rotated. Similarly, the rotation into the epineutral direction for use in a z coordinate model follows the standard (10) and (11) and requires no further information.

We provisionally recommend setting S_H and S_H^* equal to each other, as is often done in modern ocean modeling (Smith & Gent, 2004). The vertical structure of S_H^* may later be altered by methods to taper the GM fluxes to zero at the surface and bottom boundaries (e.g., Ferrari et al., 2008, 2010) without affecting the horizontal anisotropy.

5. Conclusion

In this work a global eddy-resolving ocean model has been used to diagnose the eddy transport tensor, **K**, which describes the combined effect of eddy stirring and diffusion. An inversion method using multiple tracers, pioneered in Bachman and Fox-Kemper (2013), has been employed to solve for the tensor in a least squares sense and provides a highly accurate diagnosis of the tensor, its structure, and its eigendecomposition. A previous study by Fox-Kemper et al. (2013) was a precursor to the present work but used an unoptimized version of the multiple-tracers method. The present work aimed to revisit this study and reanalyze several aspects of the solution using improvements to both the theory and diagnosis.

The emphasis here is on the diagnosis of the 2×2 horizontal/epineutral, symmetric subtensor \mathbf{S}_H , whose structure determines the anisotropy of both the eddy diffusion (Redi) and stirring (GM). Starting from a generic horizontal mixing tensor in neutral coordinates, it was shown that the eigenvalues of \mathbf{S}_H are the same as for the full 3-D symmetric tensor if the diabatic effects are small. This simplification makes it possible to perform the eigenanalysis only on \mathbf{S}_H . Using the optimized inversion method, several diagnoses were made of the full eddy transport tensor, and among these the solution with only positive eigenvalues for \mathbf{S}_H was used for further study.

The anisotropy of \mathbf{S}_H , as determined by the ratio of its eigenvalues, was found to approximately follow an exponential distribution at each vertical level. Its eigenvectors were predominantly oriented such that the major axis was aligned with the mean flow and its minor axis along the local PV gradient. An explicit relationship was derived between the vertical structures of the GM and Redi eigenvalues, which were generally found to be very similar in magnitude at all depths. The minor eigenvalues of GM and Redi were found to agree well with the GM coefficient proposed by Marshall et al. (2012). Collectively, these pieces were used to advocate for a horizontally anisotropic extension of the GM and Redi closures, and a recipe was developed for its use in ocean circulation models.

The continual refinement of mesoscale eddy closures has led to substantial improvements in the fidelity of global ocean models, and computational constraints will force the scientific community to rely on these closures for the foreseeable future. This work has aimed to provide guidance for a new generation of closures

BACHMAN ET AL. 20 of 24



which pay closer attention to their spatial orientation and physical mechanisms as well as their magnitudes. Further opportunities to refine this work exist, namely, to better understand the underlying physical mechanisms which lead to anisotropic transport. The diagnosis here likely captures many such mechanisms but cannot untangle them from one another, meaning that a more systematic approach is necessary to study each in isolation. It is possible that these studies could lead to further refinements of the anisotropic GM-Redi closure presented here. Testing of the closure is beyond the scope of this work, but would also be of significant interest.

Appendix A: The Modified Multiple-Tracers Inversion Method

In the tracer-based inversion method introduced in Bachman and Fox-Kemper (2013), the multiple-tracers flux-gradient relationship is written

$$\overline{u_i'\tau_{\beta}'} = -K_{ij}\bar{\tau}_{\beta,j},\tag{A1}$$

where Roman indices (i, j) indicate coordinates and β indicates tracer number, so that **K** contains $i \times j$ unknowns and the tracer gradient matrix contains $\beta \times j$ elements. Consecutive characters in a subscript indicate a second-order tensor, and a comma in the subscript indicates a partial derivative taken over the index following the comma. As long as the tracer gradient matrix is nonsingular one may apply a Moore-Penrose pseudoinversion Moore (1920, denoted by a superscript \dagger) to obtain a solution for **K** of the form

$$K_{ij} = -\overline{u_i'\tau_{\beta}'} \left[\bar{\tau}_{\beta,j} \right]^{\dagger}. \tag{A2}$$

An important nuance of this method is that the tracer gradients must remain misaligned for (A2) to yield a solution, which is difficult to enforce in models running for a long period of time. Since the action of the diffusive tensor **S** tends to align the tracer isosurfaces with the major principal axis, even in nonstationary flow the tracer gradients will become more colinear over time. One way of maintaining the necessary misalignment of the tracer gradients is to add a small damping of tracer concentration to (2) via a "restoring term" $\bar{F} = \lambda_{\beta} \left(\bar{\tau} - \tau_{o} \right)$ (Plumb, 1979; Plumb & Mahlman, 1987). Here λ_{β}^{-1} is a restoring timescale, which is chosen to be unique to each tracer and is assumed small compared to the eddy turnover time, and τ_{0} is the tracer concentration at the beginning of the simulation. However, this technique also has the undesirable effect of contaminating the diagnosis (A2), since the nonconservative term \bar{F} is an irreversible sink of tracer variance.

Bachman et al. (2015) introduced a means of accounting for and removing the effects of this sink by assuming that it contributes linearly to the flux-gradient relation (A1) (e.g., Plumb & Mahlman, 1987), which is now written as

$$\overline{\mathbf{u}'\tau'} = -(\mathbf{K} + \lambda \mathbf{D}) \cdot \nabla \bar{\tau}. \tag{A3}$$

The matrix \mathbf{D} consists of correlations between parcel displacements (Plumb & Mahlman, 1987) and is assumed to capture the bulk of the dependence on the tracer relaxation. It is important to note that, as with the derivation of the linear flux-gradient relation (4), the linear contribution of \mathbf{D} is only formally valid in the limit of small-amplitude parcel displacements (Plumb, 1979). The work here makes the usual assumption, without proof, that this form generalizes to large-amplitude, nonlinear eddy fluxes. As the nine passive tracers in the global model use this restoration method to keep their gradients misaligned, the basic technique described in Bachman et al. (2015) is modified and employed as follows.

The flux-gradient relation (4) for each of the nine tracer equations amounts to 27 equations in total, which are

$$\overline{u_i'\tau_\gamma'} = -(K_{ij} + \lambda_\gamma D_{ij})\bar{\tau}_{\gamma,j} + \eta_{i\gamma} \tag{A4}$$

$$\overline{u_i'\tau_\mu'} = -(K_{ij} + \lambda_\mu D_{ij})\bar{\tau}_{\mu,j} + \eta_{i\mu} \tag{A5}$$

BACHMAN ET AL. 21 of 24

$$\overline{u_i'\tau_v'} = -(K_{ij} + 0)\bar{\tau}_{v,j} + \eta_{iv}. \tag{A6}$$

The subscripts γ , μ , and ν are tracer indices used to differentiate tracers from each of three sets, such that $1 \le \gamma \le 3$, $4 \le \mu \le 6$, and $7 \le \nu \le 9$. Set γ uses a restoring timescale $\lambda_{\gamma}^{-1} = 180$ days, set μ uses $\lambda_{\mu}^{-1} = 360$ days, and set ν is unrestored. The noise terms η are present to make each equation exact and represent the quality of the diagnosis of \mathbf{K} ; a perfect diagnosis would make the flux-gradient relation exact and $\eta = 0$, so the goal is to minimize η by skillful employment of the pseudoinversion techniques. The use of extra tracers, the elimination of the relaxation terms \mathbf{D} (described below), and extra sampling depicted in Figure 1 all contribute to this minimization.

The pseudoinversion (A2) can be performed on each of the three sets independently, still leaving 27 equations:

$$\overline{u_i'\tau_\gamma'}(\bar{\tau}_{\gamma,j})^{\dagger} = -(K_{ij} + \lambda_\gamma D_{ij}) + \eta_{i\gamma}(\bar{\tau}_{\gamma,j})^{\dagger}$$
(A7)

$$\overline{u_i'\tau_\mu'}\big(\bar{\tau}_{\mu,j}\big)^\dagger = -(K_{ij} + \lambda_\mu D_{ij}) + \eta_{i\mu}\big(\bar{\tau}_{\mu,j}\big)^\dagger \tag{A8}$$

$$\overline{u_i'\tau_v'}\big(\bar{\tau}_{v,j}\big)^{\dagger} = -(K_{ij} + 0) + \eta_{iv}\big(\bar{\tau}_{v,j}\big)^{\dagger}. \tag{A9}$$

The linearity of the \mathbf{D} contribution to (A4) and (A5) can be exploited by cross-multiplying the restoring timescales,

$$\lambda_{\mu}\overline{u_{i}^{\prime}\tau_{\gamma}^{\prime}}\left(\bar{\tau}_{\gamma,j}\right)^{\dagger} = -(\lambda_{\mu}K_{ij} + \lambda_{\gamma}\lambda_{\mu}D_{ij}) + \lambda_{\mu}\eta_{i\gamma}\left(\bar{\tau}_{\gamma,j}\right)^{\dagger} \tag{A10}$$

$$\lambda_{\gamma} \overline{u_{i}' \tau_{\mu}'} (\bar{\tau}_{\mu,j})^{\dagger} = -(\lambda_{\gamma} K_{ij} + \lambda_{\gamma} \lambda_{\mu} D_{ij}) + \lambda_{\gamma} \eta_{i\mu} (\bar{\tau}_{\mu,j})^{\dagger}$$
(A11)

$$\overline{u_i'\tau_\nu'}\big(\bar{\tau}_{\nu,j}\big)^\dagger = -(K_{ij} + 0) + \eta_{i\nu}\big(\bar{\tau}_{\nu,j}\big)^\dagger, \tag{A12}$$

after which subtraction eliminates the terms involving **D**:

$$\lambda_{\mu}\overline{u_{i}'\tau_{\gamma}'}(\bar{\tau}_{\gamma,j})^{\dagger} - \lambda_{\gamma}\overline{u_{i}'\tau_{\mu}'}(\bar{\tau}_{\mu,j})^{\dagger} = -(\lambda_{\mu} - \lambda_{\gamma})K_{ij} + \lambda_{\mu}\eta_{i\gamma}(\bar{\tau}_{\gamma,j})^{\dagger} - \lambda_{\gamma}\eta_{i\mu}(\bar{\tau}_{\mu,j})^{\dagger}$$
(A13)

$$\overline{u_i'\tau_\nu'}(\bar{\tau}_{\nu,j})^{\dagger} = -(K_{ij} + 0) + \eta_{i\nu}(\bar{\tau}_{\nu,j})^{\dagger}. \tag{A14}$$

The consequence of this subtraction is that it has reduced the original 27 equations to 18, effectively eliminating nine constraints that could be used to improve the diagnosis. The missing equations can be recovered by right-multiplying (A13) by $\bar{\tau}_{\gamma,j}$ and $\bar{\tau}_{\mu,j}$ separately, and dividing by $\lambda_{\mu} - \lambda_{\gamma}$ yields a system of 27 modified flux-gradient relations that are independent of **D**:

$$\frac{\lambda_{\mu}\overline{u_{i}'\tau_{\gamma}'} - \lambda_{\gamma}\overline{u_{i}'\tau_{\mu}'}(\bar{\tau}_{\mu,j})^{\dagger}\bar{\tau}_{\gamma,j}}{\lambda_{\mu} - \lambda_{\gamma}} = -K_{ij}\bar{\tau}_{\gamma,j} + \frac{\lambda_{\mu}\eta_{i\gamma} - \lambda_{\gamma}\eta_{i\mu}(\bar{\tau}_{\mu,j})^{\dagger}\bar{\tau}_{\gamma,j}}{\lambda_{\mu} - \lambda_{\gamma}}$$
(A15)

$$\frac{\lambda_{\mu}\overline{u_{i}'\overline{v_{\gamma}'}}(\bar{\tau}_{\gamma,j})^{\dagger}\bar{\tau}_{\mu,j} - \lambda_{\gamma}\overline{u_{i}'\overline{v_{\mu}'}}}{\lambda_{\mu} - \lambda_{\gamma}} = -K_{ij}\bar{\tau}_{\mu,j} + \frac{\lambda_{\mu}\eta_{i\gamma}(\bar{\tau}_{\gamma,j})^{\dagger}\bar{\tau}_{\mu,j} - \lambda_{\gamma}\eta_{i\mu}}{\lambda_{\mu} - \lambda_{\gamma}}$$
(A16)

$$\overline{u_i'\tau_\nu'} = -K_{ij}\bar{\tau}_{\nu,j} + \eta_{i\nu}. \tag{A17}$$

Note that the noise terms η have been reweighted but are of the same magnitude as in the original sets (A4)–(A6). Performing a full pseudoinversion using the 27 equations in (20)–(22) leads to a solution for **K** that is largely free of the tracer restoring effects, but whose convergence properties are no worse than the same operation on the unmodified equations.

BACHMAN ET AL. 22 of 24



Acknowledgments

We would like to thank Dhruv Balwada and two anonymous reviewers for comments which greatly improved this manuscript. This material is based upon work supported by the National Center for Atmospheric Research (NCAR), which is a major facility sponsored by the National Science Foundation under Cooperative Agreement 1852977. We would like to acknowledge high-performance computing support from Cheyenne (doi:10.5065/D6RX99HX) provided by NCAR's Computational and Information Systems Laboratory, sponsored by the National Science Foundation. The model data and postprocessing scripts used for this research are publicly available at the Brown University Digital Repository (https://doi.org/10.7301/Z0R20Z96).

References

- Abernathey, R., Ferreira, D., & Klocker, A. (2013). Diagnostics of isopycnal mixing in a circumpolar channel. *Ocean Modelling*, 72, 1–16. https://doi.org/10.1016/j.ocemod.2013.07.004
- Adcroft, A., Hill, C., & Marshall, J. (1997). Representation of topography by shaved cells in a height coordinate ocean model. *Monthly Weather Review*, 125(9), 2293–2315. https://doi.org/10.1175/1520-0493(1997)125h2293:ROTBSCi2.0.CO;2
- Antonov, J. I., & Levitus, S. (2006). World Ocean Atlas 2005. Vol. 2, Salinity.
- Bachman, S., & Fox-Kemper, B. (2013). Eddy parameterization challenge suite I: Eady spindown. *Ocean Modelling*, 64, 12–28. https://doi.org/10.1016/j.ocemod.2012.12.003
- Bachman, S., Fox-Kemper, B., & Bryan, F. (2015). A tracer-based inversion method for diagnosing eddy-induced diffusivity and advection. Ocean Modelling, 86, 1–14. https://doi.org/10.1016/j.ocemod.2014.11.006
- Bachman, S., Marshall, D., Maddison, J., & Mak, J. (2017). Evaluation of a scalar eddy transport coefficient based on geometric constraints. Ocean Modelling, 109, 44–54. https://doi.org/10.1016/j.ocemod.2016.12.004
- Batchelor, G. (1949). Diffusion in a field of homogeneous turbulence. I. Eulerian analysis. *Australian Journal of Chemistry*, 2(4), 437–450. https://doi.org/10.1071/CH9490437
- Bryan, F., & Bachman, S. (2015). Isohaline salinity budget of the North Atlantic salinity maximum. *Journal of Physical Oceanography*, 45(3), 724–736. https://doi.org/10.1175/JPO-D-14-0172.1
- Bryden, H., & Brady, E. (1989). Eddy momentum and heat fluxes and their effects on the circulation of the equatorial Pacific Ocean. *Journal of Marine Research*, 47(1), 55–79.
- Cessi, P. (2008). An energy-constrained parameterization of eddy buoyancy flux. *Journal of Physical Oceanography*, 38(8), 1807–1819. https://doi.org/10.1175/2007JPO3812.1
- Chelton, D., Schlax, M., & Samelson, R. (2011). Global observations of nonlinear mesoscale eddies. *Progress in Oceanography*, 91(2), 167–216. https://doi.org/10.1016/j.pocean.2011.01.002
- Chelton, D., Schlax, M., Samelson, R., & de Szoeke, R. (2007). Global observations of large oceanic eddies. *Geophysical Research Letters*, 34, L15606. https://doi.org/10.1029/2007GL030812
- Danabasoglu, G., & Marshall, J. (2007). Effects of vertical variations of thickness diffusivity in an ocean general circulation model. *Ocean Modelling*, 18(2), 122–141. https://doi.org/10.1016/j.ocemod.2007.03.006
- Davis, R. (1987). Modeling eddy transport of passive tracers. Journal of Marine Research, 45(3), 635-666. https://doi.org/10.1357/002224087788326803
- Dukowicz, J., & Smith, R. (1997). Stochastic theory of compressible turbulent fluid transport. *Physics of Fluids*, 9(11), 3523–3529. https://doi.org/10.1063/1.869460
- Eden, C., & Greatbatch, R. (2008). Towards a mesoscale eddy closure. Ocean Modelling, 20(3), 223–239. https://doi.org/10.1016/j.ocemod.
- Eden, C., Jochum, M., & Danabasoglu, G. (2009). Effects of different closures for thickness diffusivity. *Ocean Modelling*, 26(1-2), 47–59. https://doi.org/10.1016/j.ocemod.2008.08.004
- Ferrari, R., Griffies, S., Nurser, G., & Vallis, G. (2010). A boundary-value problem for the parameterized mesoscale eddy transport. *Ocean Modelling*, 32(3-4), 143–156. https://doi.org/10.1016/j.ocemod.2010.01.004
- Ferrari, R., McWilliams, J., Canuto, V., & Dubovikov, M. (2008). Parameterization of eddy fluxes near oceanic boundaries. *Journal of Climate*, 21(12), 2770–2789. https://doi.org/10.1175/2007JCLI1510.1
- Ferrari, R., & Nikurashin, M. (2010). Suppression of eddy diffusivity across jets in the Southern Ocean. *Journal of Physical Oceanography*, 40(7), 1501–1519. https://doi.org/10.1175/2010JPO4278.1
- Fox-Kemper, B., Ferrari, R., & Hallberg, R. (2008). Parameterization of mixed layer eddies. Part I: Theory and diagnosis. *Journal of Physical Oceanography*, 38(6), 1145–1165. https://doi.org/10.1175/2007JPO3792.1
- Fox-Kemper, B., Lumpkin, R., & Bryan, F. (2013). Lateral transport in the ocean interior. In *International geophysics* (Vol. 103, pp. 185–209). Oxford, UK and Amsterdam, The Netherlands: Elsevier. https://doi.org/10.1016/B978-0-12-391851-2.00008-8
- Fox-Kemper, B., & Menemenlis, D. (2008). Can large eddy simulation techniques improve mesoscale rich ocean models. *Ocean modeling in an eddying regime*, 177, 319–337.
- Gent, P., & McWilliams, J. (1990). Isopycnal mixing in ocean circulation models. *Journal of Physical Oceanography*, 20(1), 150–155. https://doi.org/10.1175/1520-0485(1990)020<0150:IMIOCM>2.0.CO;2
- Gent, P., Willebrand, J., McDougall, T., & McWilliams, J. (1995). Parameterizing eddy-induced tracer transports in ocean circulation models. Journal of Physical Oceanography, 25(4), 463–474. https://doi.org/10.1175/1520-0485(1995)025<0463:PEITTI>2.0.CO;2
- Green, J. (1970). Transfer properties of the large-scale eddies and the general circulation of the atmosphere. Quarterly Journal of the Royal Meteorological Society, 96(408), 157–185. https://doi.org/10.1002/qj.49709640802
- Griffies, S. (1998). The Gent–McWilliams skew flux. Journal of Physical Oceanography, 28(5), 831–841. https://doi.org/10.1175/1520 -0485(1998)028h0831:TGMSFi2.0.CO;2
- Griffies, S., Gnanadesikan, A., Pacanowski, R. C., Larichev, V., Dukowicz, J., & Smith, R. (1998). Isoneutral diffusion in a z-coordinate ocean model. Journal of Physical Oceanography, 28(5), 805–830. https://doi.org/10.1175/1520-0485(1998)028h0805:IDIAZCi2.0.CO;2
- Grooms, I., Julien, K., & Fox-Kemper, B. (2011). On the interactions between planetary geostrophy and mesoscale eddies. *Dynamics of Atmospheres and Oceans*, 51(3), 109–136. https://doi.org/10.1016/j.dynatmoce.2011.02.002
- Hallberg, R. (2013). Using a resolution function to regulate parameterizations of oceanic mesoscale eddy effects. *Ocean Modelling*, 72, 92–103. https://doi.org/10.1016/j.ocemod.2013.08.007
- Isachsen, P. (2011). Baroclinic instability and eddy tracer transport across sloping bottom topography: How well does a modified Eady model do in primitive equation simulations? *Ocean Modelling*, 39(1-2), 183–199. https://doi.org/10.1016/j.ocemod.2010.09.007
- Killworth, P. (1997). On the parameterization of eddy transfer. Part I. Theory. *Journal of Marine Research*, 55(6), 1171–1197. https://doi.org/10.1357/0022240973224102
- Klocker, A., Ferrari, R., & LaCasce, J. (2012). Estimating suppression of eddy mixing by mean flows. *Journal of Physical Oceanography*, 42(9), 1566–1576. https://doi.org/10.1175/JPO-D-11-0205.1
- Kraichnan, R. (1987). Eddy viscosity and diffusivity: Exact formulas and approximations. Complex Systems, 1(4-6), 805-820.
- LaCasce, J., & Speer, K. (1999). Lagrangian statistics in unforced barotropic flows. *Journal of Marine Research*, 57(2), 245–274. https://doi.org/10.1357/002224099321618218
- Large, W., McWilliams, J., & Doney, S. (1994). Oceanic vertical mixing: A review and a model with a nonlocal boundary layer parameterization. Reviews of Geophysics, 32(4), 363–403. https://doi.org/10.1029/94RG01872

BACHMAN ET AL. 23 of 24



- Locarnini, R., Mishonov, A., Antonov, J., Boyer, T., Garcia, H., Baranova, O., et al. (2013). World Ocean Atlas 2013. Volume 1, Temperature. Mak, J., Maddison, J., & Marshall, D. (2016). A new gauge-invariant method for diagnosing eddy diffusivities. *Ocean Modelling*, 104, 252–268. https://doi.org/10.1016/j.ocemod.2016.06.006
- Mak, J., Marshall, D., Maddison, J., & Bachman, S. (2017). Emergent eddy saturation from an energy constrained eddy parameterisation. Ocean Modelling, 112, 125–138. https://doi.org/10.1016/j.ocemod.2017.02.007
- Maltrud, M., & McClean, J. (2005). An eddy resolving global 1/10 ocean simulation. Ocean Modelling, 8(1-2), 31–54. https://doi.org/10. 1016/j.ocemod.2003.12.001
- Marshall, D., Maddison, J., & Berloff, P. (2012). A framework for parameterizing eddy potential vorticity fluxes. *Journal of Physical Oceanography*, 42(4), 539–557.
- McDougall, T. (1987). Neutral surfaces. *Journal of Physical Oceanography*, 17(11), 1950–1964. https://doi.org/10.1175/1520-0485(1987) 017h1950:NSi2.0.CO;2
- McGillicuddy, D., Anderson, L., Bates, N., Bibby, T., Buesseler, K., Carlson, C., et al. (2007). Eddy/wind interactions stimulate extraordinary mid-ocean plankton blooms. *Science*, 316(5827), 1021–1026. https://doi.org/10.1126/science.1136256
- Mechoso, C. (1980). Baroclinic instability of flows along sloping boundaries. *Journal of the Atmospheric Sciences*, 37(6), 1393–1399. https://doi.org/10.1175/1520-0469(1980)037h1393:BIOFASi2.0.CO;2
- Moore, E. (1920). On the reciprocal of the general algebraic matrix. Bulletin of the American Mathematical Society, 26, 394–395. https://doi.org/10.1090/S0002-9904-1920-03322-7
- Nakamura, N. (2001). A new look at eddy diffusivity as a mixing diagnostic. Journal of the atmospheric sciences, 58(24), 3685–3701. https://doi.org/10.1175/1520-0469(2001)058<3685;ANLAED>2.0.CO:2
- Okubo, A. (1967). The effect of shear in an oscillatory current on horizontal diffusion from an instantaneous source. *International Journal of Oceanology and Limnology*, 1(3), 194–204.
- Plumb, A. (1979). Eddy fluxes of conserved quantities by small-amplitude waves. *Journal of the Atmospheric Sciences*, 36(9), 1699–1704. https://doi.org/10.1175/1520-0469(1979)036h1699:EFOCQBi2.0.CO;2
- Plumb, A., & Ferrari, R. (2005). Transformed Eulerian-mean theory. Part I: Nonquasigeostrophic theory for eddies on a zonal-mean flow. Journal of Physical Oceanography, 35(2), 165–174. https://doi.org/10.1175/JPO-2669.1
- Plumb, A., & Mahlman, J. (1987). The zonally averaged transport characteristics of the GFDL general circulation/transport model. *Journal of the Atmospheric Sciences*, 44(2), 298–327. https://doi.org/10.1175/1520-0469(1987)044h0298:TZATCOi2.0.CO;2
- Redi, M. (1982). Oceanic isopycnal mixing by coordinate rotation. Journal of Physical Oceanography, 12(10), 1154–1158. https://doi.org/10.1175/1520-0485(1982)012h1154:OIMBCRi2.0.CO:2
- Rogerson, A., Miller, P., Pratt, L., & Jones, C. (1999). Lagrangian motion and fluid exchange in a barotropic meandering jet. *Journal of Physical Oceanography*, 29(10), 2635–2655. https://doi.org/10.1175/1520-0485(1999)029h2635:LMAFEIi2.0.CO;2
- Smith, R. D. (1999). The primitive equations in the stochastic theory of adiabatic stratified turbulence. *Journal of Physical Oceanography*, 29(8), 1865–1880. https://doi.org/10.1175/1520-0485(1999)029h1865:TPEITSi2.0.CO;2
- Smith, K. S. (2005). Tracer transport along and across coherent jets in two-dimensional turbulent flow. *Journal of Fluid Mechanics*, 544, 133–142. https://doi.org/10.1017/S0022112005006750
- Smith, R. D., & Gent, P. (2004). Anisotropic Gent–McWilliams parameterization for ocean models. *Journal of Physical Oceanography*, 34(11), 2541–2564. https://doi.org/10.1175/JPO2613.1
- Smith, R., Jones, P., Briegleb, B., Bryan, F., Danabasoglu, G., Dennis, J., et al. (2010). The parallel ocean program (POP) reference manual: Ocean component of the community climate system model (CCSM) and community earth system model (CESM). *Rep. LAUR-01853*, 141. 1–140.
- Smith, R. D., Kortas, S., & Meltz, B. (1995). Curvilinear coordinates for global ocean models. Los Alamos preprint LA-UR-95-1146.
- Smith, K. S., & Marshall, J. (2009). Evidence for enhanced eddy mixing at middepth in the Southern Ocean. *Journal of Physical Oceanography*, 39(1), 50-69. https://doi.org/10.1175/2008JPO3880.1
- Srinivasan, K., & Young, W. (2014). Reynolds stress and eddy diffusivity of β -plane shear flows. *Journal of the Atmospheric Sciences*, 71(6), 2169–2185. https://doi.org/10.1175/JAS-D-13-0246.1
- Starr, V. (1966). Physics of negative viscosity phenomena. Earth and Planetary Science Series, 256.
- Taylor, G. (1922). Diffusion by continuous movements. *Proceedings of the London Mathematical Society*, 2(1), 196–212. https://doi.org/10.1112/plms/s2-20.1.196
- Taylor, G. (1953). Dispersion of soluble matter in solvent flowing slowly through a tube. *Proceedings of the Royal Society of London. Series A. Mathematical and Physical Sciences*, 219(1137), 186–203.
- Taylor, G. (1954). The dispersion of matter in turbulent flow through a pipe. Proceedings of the Royal Society of London. Series A. Mathematical and Physical Sciences, 223(1155), 446–468. https://doi.org/10.1098/rspa.1953.0139
- Vallis, G. (2017). Atmospheric and oceanic fluid dynamics. Cambridge, UK: Cambridge University Press.
- Veronis, G. (1975). The role of models in tracer studies. In *Numerical Models of Ocean Circulation* (pp. 133–146). Washington, DC: Natl. Acad. of Sci.
- Visbeck, M., Marshall, J., Haine, T., & Spall, M. (1997). Specification of eddy transfer coefficients in coarse-resolution ocean circulation models. *Journal of Physical Oceanography*, 27(3), 381–402. https://doi.org/10.1175/1520-0485(1997)027<0381:SOETCI>2.0.CO;2
- Von Storch, J.-S., Eden, C., Fast, I., Haak, H., Hernández-Deckers, D., Maier-Reimer, E., et al. (2012). An estimate of the Lorenz energy cycle for the world ocean based on the STORM/NCEP simulation. *Journal of Physical Oceanography*, 42(12), 2185–2205. https://doi.org/10.1175/JPO-D-12-079.1
- Welander, P. (1971). A discussion on ocean currents and their dynamics—The thermocline problem. *Philosophical Transactions of the Royal Society of London, Series A. Mathematical and Physical Sciences*, 270(1206), 415–421, https://doi.org/10.1098/rsta.1971.0081
- Wilson, C., & Williams, R. G. (2006). When are eddy tracer fluxes directed downgradient? *Journal of Physical Oceanography*, 36(2), 189–201. https://doi.org/10.1175/JPO2841.1
- Wolfram, P., Ringler, T. D., Maltrud, M. E., Jacobsen, D. W., & Petersen, M. R. (2015). Diagnosing isopycnal diffusivity in an eddying, idealized midlatitude ocean basin via Lagrangian, in Situ, Global, High-Performance Particle Tracking (LIGHT). *Journal of Physical Oceanography*, 45(8), 2114–2133. https://doi.org/10.1175/JPO-D-14-0260.1
- Young, W., Rhines, P., & Garrett, C. (1982). Shear-flow dispersion, internal waves and horizontal mixing in the ocean. *Journal of Physical Oceanography*, 12(6), 515–527. https://doi.org/10.1175/1520-0485(1982)012h0515:SFDIWAi2.0.CO;2

BACHMAN ET AL. 24 of 24